Properties of Plasma Waves Observed Upstream From Mars

J. S. Halekas, S. Ruhunusiri, O. L. Vaisberg, Y. Harada, J. R. Espley, D. L. Mitchell, C. Mazelle, N. Romanelli, G. A. Dibraccio, D. A. Brain

Correspondence to:
J. S. Halekas,
jasper-halekas@uiowa.edu

Properties of Plasma Waves Observed Upstream From Mars

J. S. Halekas[1] [ID], S. Ruhunusiri[1] [ID], O. L. Vaisberg[2] [ID], Y. Harada[3] [ID], J. R. Espley[4], D. L. Mitchell[5] [ID], C. Mazelle[6] [ID], N. Romanelli[4,7] [ID], G. A. DiBraccio[4] [ID], and D. A. Brain[8] [ID]

[1]Department of Physics and Astronomy, University of Iowa, Iowa City, IA, USA, [2]Space Research Institute, Russian Academy of Sciences, Moscow, Russia, [3]Department of Geophysics, Kyoto University, Kyoto, Japan, [4]NASA Goddard Space Flight Center, Greenbelt, MD, USA, [5]Space Sciences Laboratory, University of California, Berkeley, CA, USA, [6]IRAP, University of Toulouse, Toulouse, France, [7]CRESST II, University of Maryland, Baltimore, MD, USA, [8]Laboratory for Atmospheric and Space Physics, University of Colorado, Boulder, CO, USA

Abstract We describe a new method to analyze the properties of plasma waves and apply it to observations made upstream from Mars by the Mars Atmosphere and Volatile EvolutioN (MAVEN) mission. The slow measurement cadence of most charged particle instrumentation has limited the application of analysis techniques based on correlations between particle and magnetic field measurements. We show that we can extend the frequency range of applicability for these techniques, for a subset of waves that remain nearly coherent over multiple wave periods, by subsampling velocity distribution function measurements and binning them by the wave phase. This technique enables the computation of correlations and transport ratios for plasma waves previously inaccessible to this technique at Mars. By computing the cross helicity, we find that most identified waves propagate upstream in the plasma frame. This supports the conclusions of previous studies but enables a clearer determination of the intrinsic wave mode and characteristics. The intrinsic properties of observed waves with frequencies close to the proton cyclotron frequency have little spatial variability but do have large temporal variations, likely due to seasonal changes in the hydrogen exosphere. In contrast, the predominant characteristics of waves at higher frequencies have less temporal variability but more spatial variability. We find several indications of the presence of multiple wave modes in the lower frequency wave observations, with unusual wave properties observed for propagation parallel to the magnetic field and for background magnetic fields nearly perpendicular to the solar wind flow.

Plain Language Summary The interaction between the solar wind and planetary environments leads to the growth of a variety of plasma waves. These waves serve as a sensitive tracer of the physical interactions between the solar wind and local charged particle populations. Plasma waves reveal the conversion of energy between kinetic and electromagnetic forms, as well as mediating the exchange of energy between different particle populations. However, identifying the intrinsic characteristics of low-frequency plasma waves often proves quite challenging, because the solar wind sweeps them downstream, altering their properties as measured by an orbiting spacecraft. By combining magnetic field and charged particle data, one can remove some of the resulting ambiguities. However, the low cadence of many charged particle observations limits the applicability of such analyses. In this work, we describe a new technique to eke higher time resolution out of the charged particle measurements and apply it to observations from the Mars Atmosphere and Volatile EvolutioN (MAVEN) mission, opening a new window on the properties of plasma waves at Mars.

1. Introduction

Mars, though lacking a global intrinsic magnetic field, has a magnetosphere bounded by a bow shock and magnetosheath (Dubinin et al., 2006; Halekas et al., 2017; Nagy et al., 2004). The region upstream from Mars contains a number of distinct charged particle populations, many of which have free energy that can lead to the growth of plasma waves (Dubinin & Fraenz, 2016; Mazelle et al., 2004). Like other objects with a bow shock, Mars has a foreshock region extending upstream from the shock. The foreshock contains unstable reflected ion and electron populations that drive plasma instabilities (Russell et al., 1990), much as in the terrestrial foreshock (Eastwood et al., 2005). In addition, Mars has neutral oxygen and hydrogen

exospheres formed by photochemical and thermal processes (Anderson et al., 1971; Feldman et al., 2011), which extend well beyond the bow shock. The ionized constituents of these exospheric populations (pickup ions) can drive plasma instabilities, much as in cometary environments (Brinca, 1991; Lee, 1989; Tsurutani, 1991). The pickup ions can themselves reflect from the shock (Dubinin et al., 2006), creating another population with free energy.

In this study, we focus on nearly coherent low-frequency electromagnetic waves with frequencies of ~0.01–10 Hz. Upstream waves in this frequency range fall into several different classes, not always clearly separated from each other. At the higher end of this frequency range, "1-Hz waves" commonly occur in planetary foreshock regions. These waves, first observed upstream from the Earth (Fairfield, 1974; Russell et al., 1971), have properties consistent with the whistler mode. They commonly have nearly circular polarization, with amplitudes of up to a few nanotesla, and propagation angles of ~10–40° to the magnetic field. They can have right- or left-handed polarization in the spacecraft frame. However, observations show that the observed polarization depends on the propagation angle with respect to the solar wind flow, in a manner consistent with intrinsic right-handed polarization in the plasma frame (Fairfield, 1974). Similar waves exist in many planetary foreshocks, including those of Mercury and Venus (Orlowski et al., 1990), Saturn (Orlowski et al., 1992), and Mars (Brain et al., 2002; Ruhunusiri et al., 2018). At Mars, their amplitude decreases with distance from the bow shock, and most occur on field lines connected to the shock (Brain et al., 2002).

At lower frequencies, "30-s waves" also commonly occur in the terrestrial foreshock (Eastwood et al., 2002; Fairfield, 1969; Hoppe & Russell, 1983; Le & Russell, 1994). These waves often have nearly circular polarization, with amplitudes up to a few nanotesla, and are thought to result from a right-hand resonant interaction with reflected ions (Barnes, 1970; Gary, 1991; Gary et al., 1981, 1984). The Doppler shift from the solar wind flow often results in an observed left-handed polarization in the spacecraft frame. The 30-s waves propagate at small oblique angles of ~10–20° to the magnetic field, despite theoretical predictions that maximum wave growth should occur for parallel propagation. Possibly, refraction can lead to the observed oblique propagation (Eastwood et al., 2004). Waves with similar properties also occur in the foreshocks of Mercury, Venus, and Mars (Dubinin & Fraenz, 2016; Guan Le et al., 2013; Romanelli et al., 2020; Ruhunusiri et al., 2016; Russell, 1994).

A particular subset of low-frequency waves, with similar properties to the 30-s waves, though typically with slightly higher frequencies in the spacecraft frame, occurs frequently at Mars. These waves have left-handed circular polarization in the spacecraft frame, with a spacecraft frame frequency equal to the local proton cyclotron frequency (Brain et al., 2002; Delva et al., 2011; Romanelli et al., 2013; Russell et al., 1990, 2006; Wei et al., 2014; Wei & Russell, 2006). Waves with similar properties occur in many locales, including Venus (Delva et al., 2008), comets (Mazelle & Neubauer, 1993), and the solar wind (Jian et al., 2014). At Mars, the observed amplitude and occurrence of these waves decrease with distance from the planet (Brain et al., 2002; Romanelli et al., 2013; Wei et al., 2014). Though often referred to as "proton cyclotron waves," they do not in fact represent ion cyclotron mode waves, which has led to some confusion. Instead, it is thought that a right-hand resonant interaction with H^+ pickup ions produced by ionization of the neutral hydrogen exosphere may generate these waves. The observed seasonal variation of their occurrence (Bertucci et al., 2013; Romanelli et al., 2016), comparable to the seasonal variation of the neutral hydrogen exosphere (Bhattacharyya et al., 2015; Chaffin et al., 2014; Halekas, 2017; Rahmati et al., 2018; Yamauchi et al., 2015), supports this hypothesis. This postulated generation mechanism closely resembles that thought to produce 30-s waves but with different relative velocities between the solar wind and the resonant population. Since the component of the velocity of the newly ionized H^+ ions along the magnetic field coincides with that of the spacecraft frame, the equality of the spacecraft frame wave frequency and the proton gyrofrequency emerges as a natural consequence of the cyclotron resonance and Doppler shift conditions (Dubinin & Fraenz, 2016). Note, however, that in the solar wind frame, the waves can have rather different frequencies.

Because the waves at the proton cyclotron frequency sometimes occur in a series of packets, with an amplitude that varies at a lower frequency, some authors have suggested that nonlinear bi-ion structures termed "oscillitons" could instead produce at least some of the observed signatures (Dubinin et al., 2004; Mazelle et al., 2004; Sauer et al., 1998, 2001; Sauer & Dubinin, 2003; Szegő et al., 2000). These structures also appear capable of reproducing many of the features of the observations, including the observed frequency near the

proton gyrofrequency. They can also have associated velocity fluctuations, albeit with a varying phase between the velocity and magnetic field fluctuations across the structure (Dubinin et al., 2004; Sauer et al., 2001; Sauer & Dubinin, 2003).

The omnipresent Doppler shift of low-frequency waves by the solar wind flow makes the identification of the intrinsic mode and characteristics of waves observed by spacecraft in the solar wind and foreshock regions difficult. Multispacecraft measurements can resolve much of this ambiguity (Eastwood et al., 2002; Hoppe & Russell, 1983), but such measurements are rarely available in planetary contexts. Instead, the identification of low-frequency wave modes typically relies on contextual information, with the derivation of the intrinsic frequency, polarization, and even propagation direction requiring assumptions based on cold plasma theory or other theoretical frameworks. A method sometimes used to resolve some of these ambiguities and identify wave modes relies on combining magnetic field and charged particle data to produce correlations and transport ratios with characteristic values and systematics for magnetohydrodynamic (MHD) modes (Gary & Winske, 1992; Song et al., 1994). One can also apply these methods to kinetic modes (Krauss-Varban et al., 1994), given appropriate data.

A previous study using measurements from the magnetometer (MAG) (Connerney et al., 2015) and Solar Wind Ion Analyzer (SWIA) (Halekas et al., 2015) instruments on the Mars Atmosphere and Volatile EvolutioN (MAVEN) mission (Jakosky et al., 2015) utilized a method based on transport ratios to identify low-frequency MHD wave modes in the Martian magnetosphere and upstream region (Ruhunusiri et al., 2015). This study found that Alfvén waves dominate both the upstream and magnetosheath regions and that fast mode waves occur frequently near the bow shock. However, the 4-s cadence of SWIA measurements limited this study to consideration of waves with spacecraft frame frequencies below 0.125 Hz.

We now describe in this paper a method to increase the frequency range of plasma waves for which we can compute correlations and transport ratios, for a subset of observed waves that remain nearly coherent over multiple wave periods. Although the intrinsic cadence of the SWIA measurements remains a limitation, we can extend our frequency coverage above the range of the instrumental energy sweep frequency by subsampling the velocity distribution function measurements and binning them by wave phase to build up a full aggregate velocity distribution for each wave phase. This technique enables the computation of correlations and transport ratios for plasma waves previously inaccessible to this technique at Mars.

2. Plasma Wave Observations Upstream From Mars

During the southern summer season, near perihelion, the Martian hydrogen exosphere reaches its most active state (Bhattacharyya et al., 2015; Chaffin et al., 2014; Halekas, 2017). Ionization of this exosphere, primarily by charge exchange with the solar wind, generates a population of H^+ ions (Rahmati et al., 2017, 2018; Yamauchi et al., 2015). These ions interact with the solar wind to generate low-frequency waves, with the same seasonal dependence as the hydrogen exosphere (Bertucci et al., 2013; Romanelli et al., 2016). In the upstream region, these waves have a ubiquitous nature during the southern summer season at Mars, and their presence can even affect the dynamics within the magnetosphere (Halekas et al., 2015).

We show typical observations during the southern summer season (solar longitude $L_S = 295°$, somewhat after perihelion $L_S = 251°$ and summer solstice at $L_S = 270°$) in Figure 1. The figure shows MAG and SWIA observations from a portion of a MAVEN orbit upstream from the bow shock, located below the southern flank of the magnetosheath, inbound toward the shock. Throughout this period, we observe coherent circularly polarized waves with left-handed polarization in the spacecraft frame, and a spacecraft frame frequency equal to the local proton cyclotron frequency. During the latter portion of the interval, we also observe broadband fluctuations, also primarily left-hand polarized in the spacecraft frame, which extend upward from the proton cyclotron frequency to a few Hz. These likely represent whistler mode waves associated with magnetic connection to the bow shock. Apparent polarization signatures at a few Hz result from reaction wheel noise but have very low power and do not affect our analysis. Both higher frequency signatures can be removed by averaging, leaving clear signatures of the waves at the proton cyclotron frequency, with consistent characteristics throughout the interval.

Contemporaneous SWIA measurements reveal that these waves have associated velocity perturbations (i.e., the cross helicity $\sigma_c = 2\langle \delta v \cdot \delta B \rangle / (\langle \delta v^2 \rangle + \langle \delta B^2 \rangle)$ is nonzero), as expected for MHD wave modes
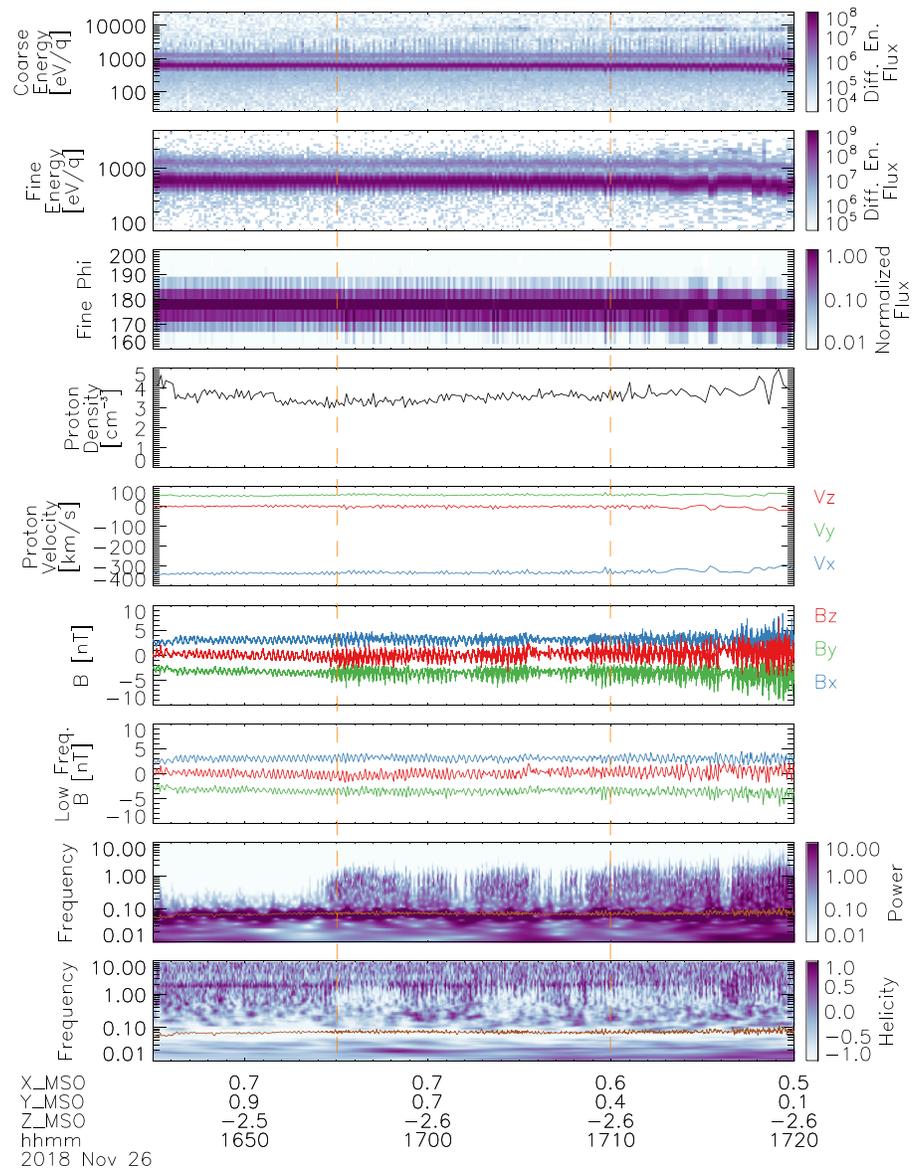
Figure 1. MAVEN observations from the SWIA and MAG instruments made upstream from the bow shock on 26 November 2018. The nine panels show coarse and fine ion energy spectra (averaged over all look angles) in units of differential energy flux (eV/[eV cm^2 s sr]), normalized ion phi angle (instrumental azimuthal angle) spectra (averaged over the fine energy range), proton density and velocity moments in Mars Solar Orbital (MSO) coordinates, full resolution (32 samples/s) vector magnetic field in MSO coordinates, vector magnetic field averaged to 2-s resolution, and magnetic field power and helicity spectra (positive values indicate right-handed polarization with respect to the background field; negative values indicate left-handed polarization) from Morlet wavelet transforms of the full resolution magnetic field components. The orange line in the bottom two panels shows the proton cyclotron frequency. The labels at the bottom indicate the universal time (UT) and MSO position of the spacecraft in units of Martian radii. The vertical dashed orange lines outline the time period analyzed in detail in Figures 4 and 5.

in which the ions move with the magnetic field lines. The velocity signatures appear as fluctuations in the solar wind core, visible in the fine mode energy and phi angle spectra. The SWIA instrument covers a three-dimensional velocity space by sweeping logarithmically in energy, sweeping in polar (deflection) angle at each energy step, and resolving azimuthal angle by the use of a segmented anode below a microchannel plate detector (Halekas, Taylor, et al., 2015). The fine mode data shown in Figure 1, which cover a subset of the full 25-eV to 25-keV energy range and 360° × 90° angular range accessible to the instrument, resolve a

limited energy and angular range centered around the instantaneous solar wind energy and angle, with 7.5% binned fractional energy resolution and ~4.5° × 4.5° angular resolution (Halekas, Taylor, et al., 2015). The moments of the proton core (computed from fine mode data) show no obvious coherent fluctuations in density but do capture the weak velocity fluctuations. The SWIA fine mode data resolve these velocity signatures rather poorly, given the velocity distribution measurement cadence of 8 s during most of this interval, which corresponds to ~2 measurements per wave period.

The SWIA coarse mode data, with the same 8-s cadence during this interval, also show some evidence of wave signatures. The coarse mode data cover the full 25-eV to 25-keV energy range and 360° × 90° angular range accessible to the instrument but sum over some resolution elements, resulting in 15% binned fractional energy resolution and ~22.5° × 22.5° angular resolution (Halekas, Taylor, et al., 2015). These data barely resolve the velocity fluctuations of the solar wind core but do reveal additional modulated signatures extending up to a few keV, potentially representing gyrophase-bunched ions. At still higher energies of ~10 keV, a population likely composed of O^+ pickup ions sporadically appears, with no apparent modulation by the waves.

During the southern winter season, both the occurrence rate and amplitude of waves at the proton cyclotron frequency decrease dramatically (Romanelli et al., 2016). The resulting reduction in turbulence in the upstream region makes the observation of higher frequency waves, notably the frequently observed whistler mode waves, more straightforward (Ruhunusiri et al., 2018). These waves, with spacecraft frame frequencies of ~0.5–3 Hz, occur commonly upstream from the Martian bow shock. Their occurrence rate has no reported seasonal dependence, and they do not correlate with the waves at the proton cyclotron frequency (Brain et al., 2002; Ruhunusiri et al., 2018). They can have a variety of polarization states in the spacecraft frame, depending on the angle between their propagation and the solar wind flow, consistent with predominantly upstream propagation of right-hand polarized waves.

We show typical observations during the southern winter season (solar longitude $L_S = 141°$, after aphelion and midway between southern winter and spring) in Figure 2. The figure shows MAG and SWIA observations from a portion of a MAVEN orbit upstream from the bow shock, located above the northern flank of the magnetosheath, outbound away from the shock. Unlike the time period of Figure 1, we do not observe either a peak in wave power or a left-handed polarization signature at the local proton cyclotron frequency. Instead, we observe a fairly broad signature of enhanced wave power between ~0.2 and 1 Hz throughout the interval, with predominantly left-handed polarization. Assuming straight line magnetic field geometry, the spacecraft should be magnetically connected to the bow shock and thus in the ion foreshock during the interval where we observe the waves. After subtracting the low-frequency component of the magnetic field to obtain a high-frequency residual, we find that these waves consist of wave trains with fairly consistent polarization. The individual waveforms have nearly circular left-handed polarization, but with substantial variability in frequency and amplitude across the interval in question, which leads to the broadband signatures in the wavelets. The relatively sharp cutoff in wave power and polarization above ~1 Hz may result from a group standing condition (Ruhunusiri et al., 2018) or from a Doppler shift effect (Fairfield, 1974).

The unprocessed SWIA measurements cannot resolve fluctuations in this frequency range, and as expected, they show no signatures of fluctuations associated with the high-frequency waves. They do show some perturbations associated with lower frequency features in the magnetic field, particularly early in the interval shown in Figure 2.

While we now understand the general properties of the two classes of waves in the region upstream from Mars shown in Figures 1 and 2 fairly well in a statistical sense, single-spacecraft magnetic field measurements alone cannot generally uniquely identify the wave mode, the propagation direction, or even the intrinsic frequency for any given observation. The calculation of correlations and transport ratios that jointly utilize magnetic field and charged particle observations could resolve some of these ambiguities. However, the sampling cadence of the MAVEN-charged particle measurements currently limits the applicability of these techniques, with the velocity distribution function measurement cadence marginal even for the lower frequency waves and completely inappropriate for the higher frequency waves. To overcome these limitations, in this study, we explore the possibility of sub-sampling the SWIA distribution measurements and aggregating them over multiple wave periods to compute average correlations and transport ratios for a subset of the observed low-frequency plasma waves.
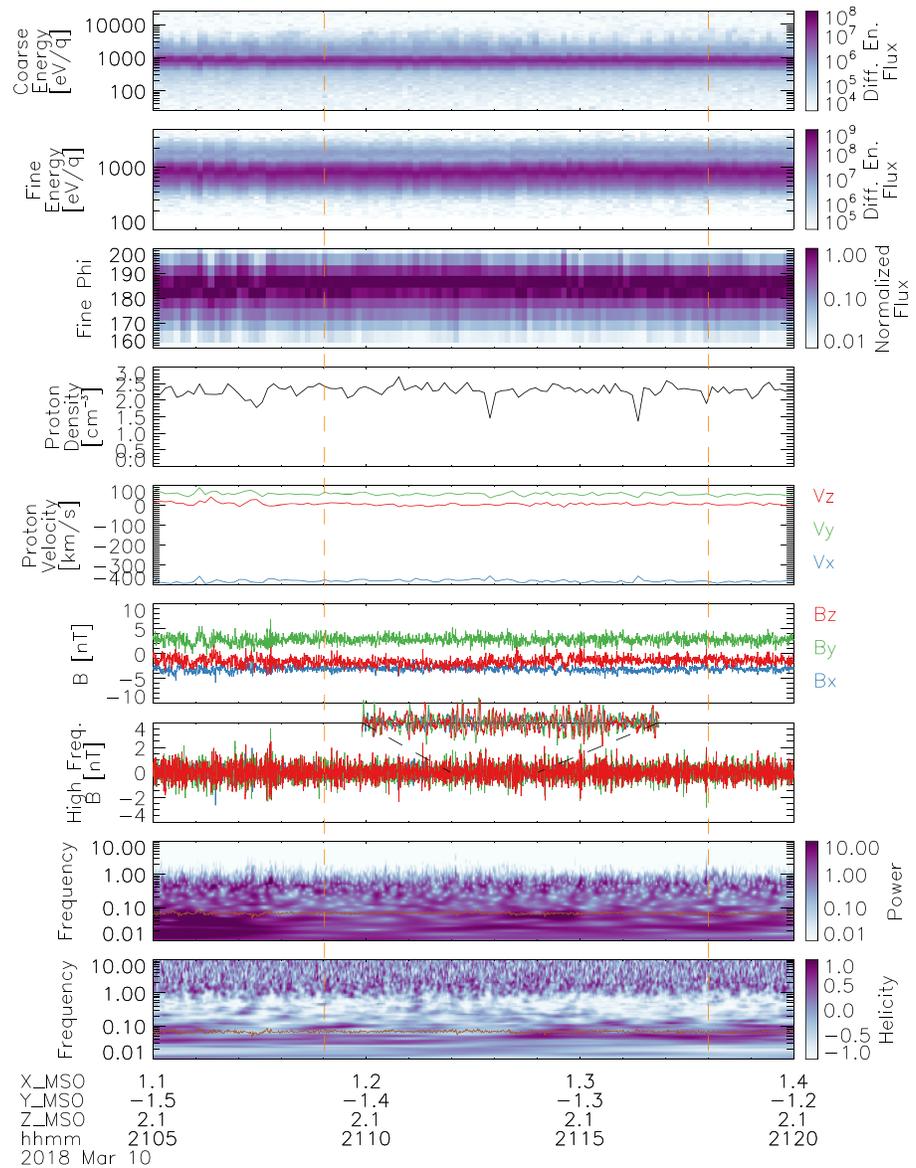
Figure 2. MAVEN observations from the SWIA and MAG instruments made upstream from the bow shock on 10 March 2018, in the same format as Figure 1, except that the seventh panel shows the high-frequency residual of the magnetic field with respect to the field averaged over 2-s intervals. An inset shows a magnified view of 2 min of this high-frequency residual field data. The vertical dashed orange lines outline the time period analyzed in detail in Figure 4.

3. Calculation of Correlations and Transport Ratios for Periodic Plasma Waves

The method we have developed to calculate correlations and transport ratios at higher time resolution, as illustrated in schematic form in Figure 3, is conceptually straightforward. Most charged particle instruments do not sample the entire velocity distribution function instantaneously but rather measure the different portions of phase space sequentially, which limits the cadence at which they measure a full distribution function. However, for a wave which remains approximately coherent (i.e., maintains nearly the same mode and polarization properties) over many wave periods, we can build up aggregate distribution functions for any given wave phase, by simply assembling all the individual distribution function measurements made at that wave phase. We can then analyze these phase-binned distribution functions just as we would a single distribution function measurement, by taking slices through velocity space, computing moments, etc. In this
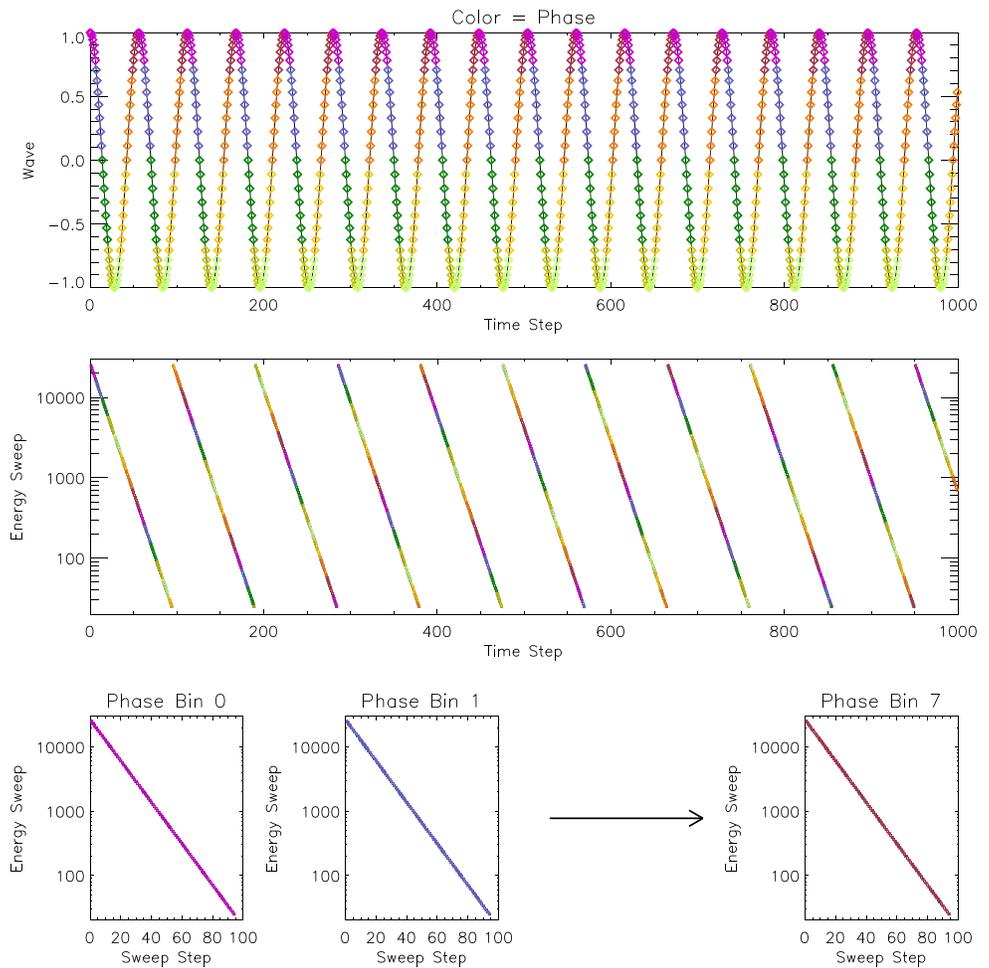
Figure 3. Schematic illustration of method for subsampling ion distributions and binning them by wave phase. The top panel shows a single magnetic field vector component (arbitrarily normalized) for a circularly polarized wave, with colors corresponding to eight wave phase bins. The second panel shows the energy sweep of the instrument on the same time scale, also colored by wave phase. The bottom row of panels shows the energy coverage obtained for selected wave phase bins by aggregating all measurements made within each wave phase bin during the time period of interest.

work, we focus primarily on the core proton population, but in principle, one could apply this method to any particle population, including minor ions or electrons.

To accomplish the phase binning, we must compute a phase for the wave as a function of time. In the example of Figure 3, one could calculate the wave phase from the single sinusoidally varying magnetic field component shown, for example, by utilizing its instantaneous magnitude and its time derivative. However, for a more realistic plasma wave, one should utilize a computation that allows for some variability in the amplitude and/or frequency of the wave, since few naturally occurring plasma waves maintain exactly the same frequency and amplitude over many wave periods. By utilizing multiple magnetic field components, we can accomplish this, as described below.

Once we obtain the phases for the wave of interest, we simply bin the individual velocity space measurements by the wave phase. SWIA and many similar analyzers utilize a logarithmically descending energy sweep, as shown in Figure 3. SWIA also sweeps in deflection angle at each energy step (with 24 deflection steps with ~1.7-ms accumulation times for each of the 96 energy steps in the instrument sweep, for a total energy step duration of ~41 ms). In contrast, most instruments on spinning spacecraft instead cover phase space by sweeping in energy and utilizing the spacecraft spin. Regardless, as long as we know the temporal sequence of phase space coverage, we can bin velocity space measurements by wave phase. In practice, one
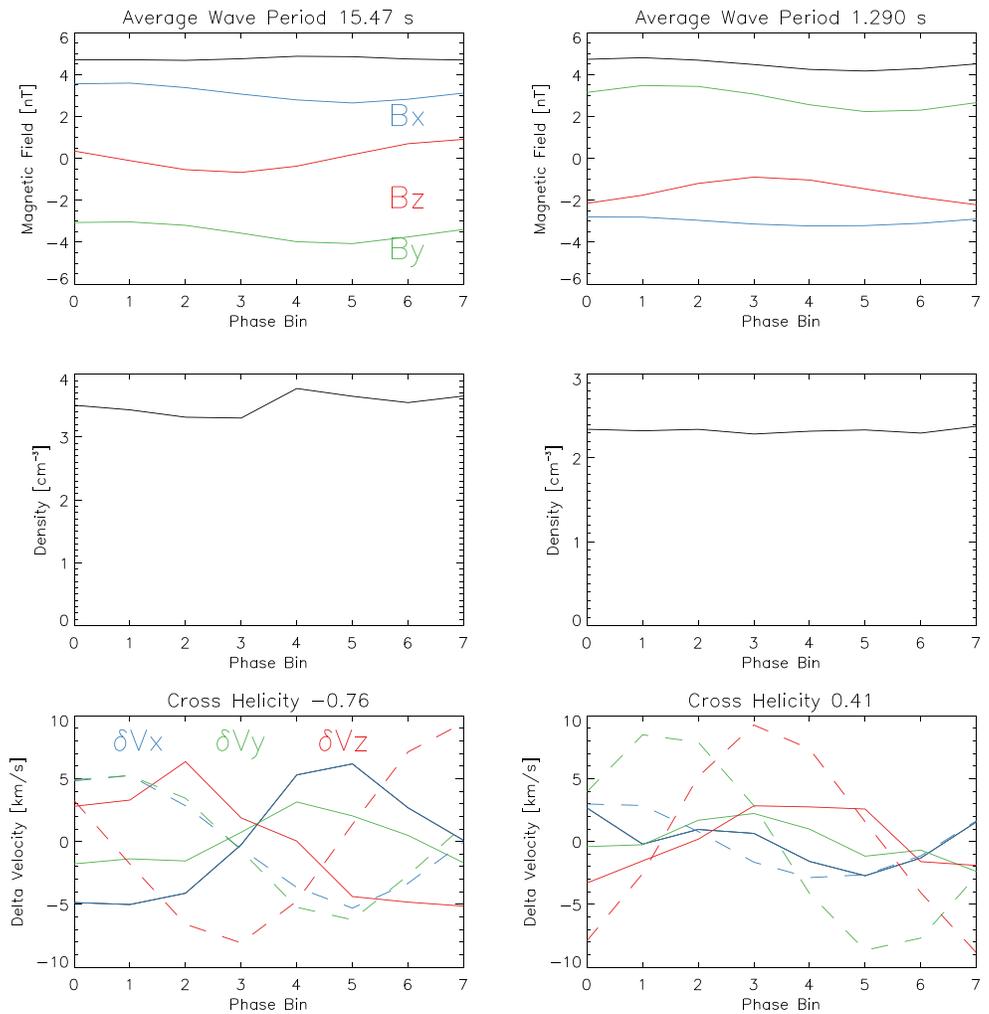
Figure 4. Phase-binned magnetic fields and proton moments computed from phase-binned SWIA fine data for the low-frequency and high-frequency waves observed in the intervals outlined in Figure 1 (left-hand column) and Figure 2 (right-hand column), respectively. The top panels show the vector magnetic field in MSO coordinates, with titles indicating the average wave period (from the derivative of the wave phase) during the interval analyzed. The middle panels show the proton density moment. The solid lines in the bottom panels show the proton velocity moments in MSO coordinates, with the average value subtracted to show the fluctuations δv. For comparison, the dashed lines show the magnetic field fluctuations δB in velocity units (obtained by dividing by the ratio of the background field magnitude and the Alfvén velocity B_0/v_A). The panel titles indicate the corresponding cross helicity $\sigma_c = 2\langle\delta v \cdot \delta B\rangle/(\langle\delta v^2\rangle + \langle\delta B^2\rangle)$.

should utilize a phase resolution adequate to resolve phase-dependent quantities, while not requiring an unrealistic number of measurements. We have found that eight wave phase bins, as shown in Figure 3, represent a reasonable compromise.

We also require an interval of sufficient duration that we can assemble an aggregate distribution function with complete velocity space coverage for each wave phase bin, as shown in Figure 3. The length of the interval required depends on both the period of the wave and the number of wave phase bins chosen for the analysis. In principle, some combinations of wave frequency and measurement duration (e.g., a wave period that contains an integer number of measurement periods) would make it impossible to utilize this technique. In practice, such cases represent only a small fraction of the observations. Furthermore, even a small level of variability in the wave frequency reduces the number of cases with an exact commensurability.

As an illustrative test, we first apply the phase binning technique described above to the observations shown in Figures 1 and 2 (using the time intervals delineated in those figures). Both cases have some complicating

factors, with wave power present at a range of frequencies, and some degree of variability in the frequency and amplitude even for the wave of interest. In presenting these examples, we thus intentionally show robust tests of our methodology, rather than utilizing the simplest possible test cases.

To compute the wave phase for these intervals, we perform several steps. First, we isolate the frequency range of interest. To analyze the low-frequency waves, we utilize 2-s averages of the instantaneous fields to remove the high-frequency components, as shown in Figure 1. We then linearly detrend the fields to remove any change in the background field over the interval of interest. To analyze the high-frequency waves, we subtract the field averaged over 2-s intervals to remove the low-frequency components (which also detrends the fields), as shown in Figure 2. One could utilize more sophisticated algorithms to high-pass or low-pass filter the fields and to detrend them, but we elect to use a very simple approach, which proves adequate for our purposes.

We next perform minimum variance analysis (Song & Russell, 1999; Sonnerup & Cahill, 1968) on the filtered magnetic fields, over the entire analysis interval, to find a principal axis coordinate system approximately aligned with the wave propagation vector (to within a 180° ambiguity). We then compute the wave phase from the field components in the principal axis coordinate system and the principal component eigenvalues as $\phi = tan^{-1}\left(\frac{B_{\text{int}}/\sqrt{\lambda_{\text{int}}}}{B_{\text{max}}/\sqrt{\lambda_{\text{max}}}}\right)$. This definition has the advantage that it remains robust even under slow variations in the wave frequency and/or amplitude. Strictly speaking, this only provides an exact phase for a perfectly planar elliptically polarized wave, with only a single mode present in the frequency range analyzed. For the waves of interest in this work, this proves a good approximation. Even for waves with some nonplanarity or nonlinearity, the computation of correlations and transport ratios remains fairly robust, since we use the same phase to bin both the magnetic field and charged particle measurements.

Figure 4 shows that the phase binning procedure described above captures a clear elliptically polarized wave in both the low-frequency and high-frequency cases. We present results for the particular time intervals delineated in Figures 1 and 2. Shifting these time intervals slightly or changing their length has no significant effects on the results shown. We use a filtered and detrended form of the magnetic field to compute the wave phase, but we utilize the full magnetic field to compute the phase-binned averages that we utilize for the calculation of correlations and transport ratios. The phase-binning process essentially selects a single Fourier component in both the magnetic field and charged particle data. For both test cases, we note a small compressional magnetic field component, consistent with slightly oblique propagation. We also find clear velocity fluctuation signatures in the phase-binned SWIA data for both cases, which we can use to compute cross helicity values and distinguish between parallel and antiparallel propagation along the magnetic field.

The low-frequency wave (left column of Figure 4) has nearly circular left-handed polarization, with a high degree of planarity, given eigenvalues from minimum variance analysis of 0.30, 0.25, and 0.0014. The wave normal angle θ_{KB} between the magnetic field and the estimated propagation direction from minimum variance is 7.1°. The wave has an RMS amplitude $<\delta\boldsymbol{B}> = 0.74$ nT and an RMS compressional amplitude $<\delta B_{\parallel}> = 0.07$ nT (fractional amplitudes of 0.16 and 0.015), consistent with the nearly field-aligned propagation. The phase-binned density for the low-frequency case also reveals a small compressional component (though not as smoothly varying as the magnetic field magnitude), with an RMS amplitude $<\delta n> = 0.16$ cm^{-3} (fractional amplitude of 0.045). The linear correlation coefficient between the magnetic field magnitude perturbation and the density perturbation is 0.64, with maximum correlation for zero phase shift between the two quantities, consistent with a fast magnetosonic mode wave. We find that the compressibility $C_{Bn} = \frac{\langle \delta n \cdot \delta n \rangle}{\langle n^2 \rangle} \cdot \frac{\langle B_0^2 \rangle}{\langle \delta\boldsymbol{B} \cdot \delta\boldsymbol{B} \rangle} = 0.08$ and the parallel compressibility $C_{\parallel} = \frac{\langle \delta n \cdot \delta B_{\parallel} \rangle}{\langle B_0 \cdot n_0 \rangle} \cdot \frac{\langle B_0^2 \rangle}{\langle \delta B_{\parallel} \cdot \delta B_{\parallel} \rangle} = 1.9$, both consistent with a fast mode magnetosonic wave, given the moderate β_i of 0.33 (Gary & Winske, 1992; Krauss-Varban et al., 1994). We find a clear anticorrelation between magnetic field and velocity fluctuations, with a cross helicity $\sigma_c = -0.76$ (Matthaeus & Goldstein, 1982), and approximately the same magnitude in Alfvén units (i.e., an Alfvén ratio R_A close to unity). This large negative cross helicity unambiguously indicates wave propagation parallel to the background magnetic field in the plasma frame (in this case in the upstream direction, given the positive B_x). These properties all therefore support the identification of an upstream-propagating fast magnetosonic mode wave (thus, with right-handed intrinsic polarization)
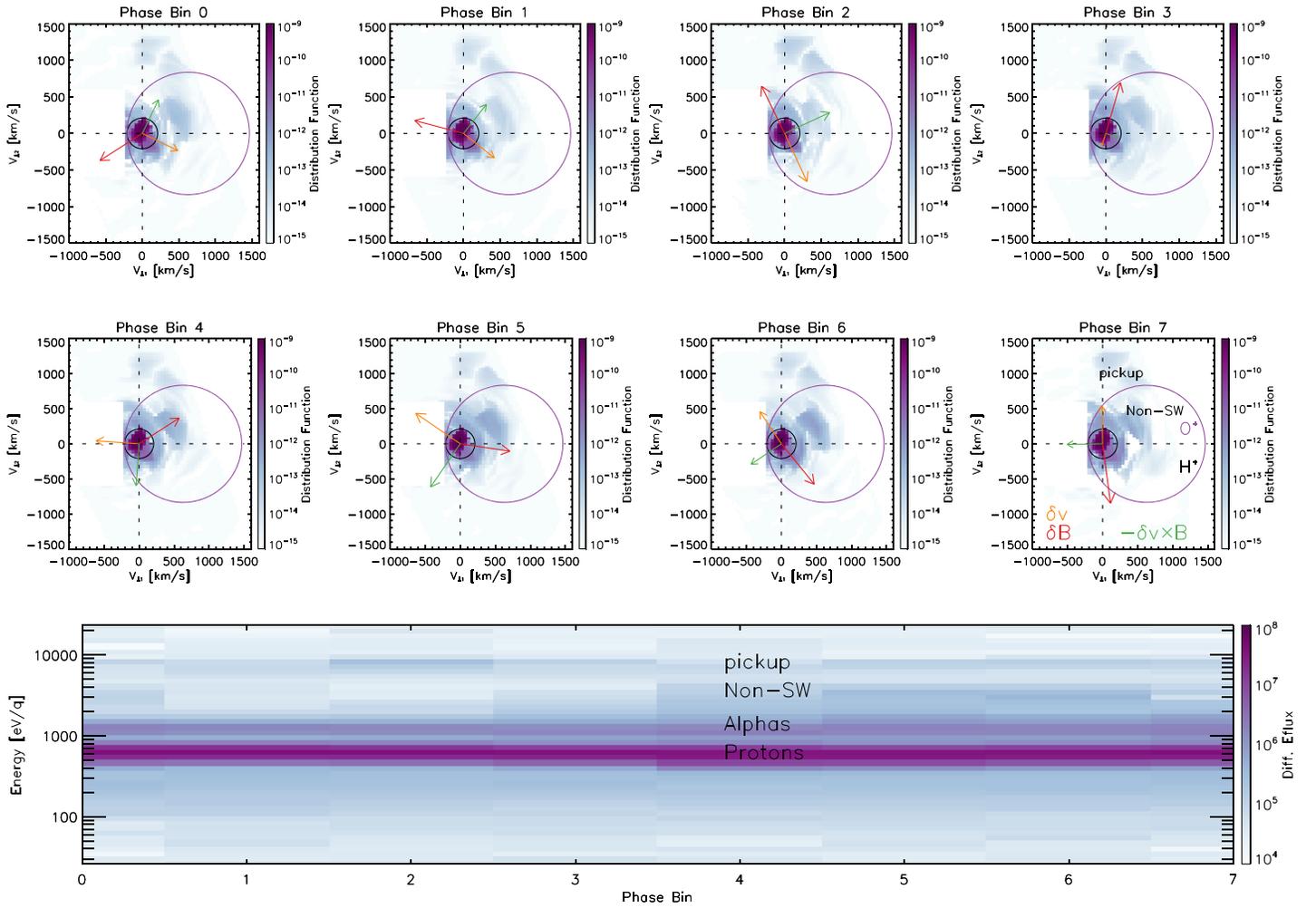
Figure 5. Phase-binned ion distributions computed from SWIA coarse data for the low-frequency waves observed in the interval outlined in Figure 1. The eight plots in the top two rows show cuts through the ion distribution function (s^3/m^6) in the plane perpendicular to the average magnetic field B_0, centered on the average proton velocity v_{SW}, with the x-axis parallel to the component of v_{SW} perpendicular to B_0, and the y-axis parallel to the average motional electric field $-v_{SW} \times B_0$. A portion of the velocity space subject to contamination by scattered particles is blanked out. The black and purple circles indicate the expected velocity space trajectories of H^+ and O^+ pickup ions. The orange, red, and green arrows show the directions and relative magnitudes of the fluctuating velocity, magnetic field, and electric field components (from data in Figure 4) in this plane. The bottom panel shows a phase-binned energy spectrum, averaged over all look angles, in units of differential energy flux (eV/[eV cm^2 s sr]).

Doppler shifted by the solar wind flow to satisfy the resonance condition with H^+ ions, resulting in the observed left-handed polarization at the proton cyclotron frequency in the spacecraft frame.

Meanwhile, the high-frequency wave (right column of Figure 4) also has nearly circular left-handed polarization and a high degree of planarity, with eigenvalues of 0.24, 0.22, and 0.000031. The wave has a larger normal angle θ_{KB} of 28.3°. The wave has a similar $<\delta B> = 0.67$ nT, but a higher $<\delta B_{||}> = 0.22$ nT (fractional amplitudes of 0.15 and 0.05), consistent with the more oblique propagation. In this case, we see no visually apparent density perturbation, with $<\delta n> = 0.03$ cm^{-3} (fractional amplitude of 0.01). The linear correlation coefficient between the magnetic field magnitude and density perturbations in this case is only 0.27, and higher correlations exist for phase shifts of 45–90°. We find a compressibility and parallel compressibility of 0.005 and 0.06 respectively, very small and likely not significant. We do, however, find an appreciable correlation between magnetic field and velocity fluctuations, with $\sigma_c = 0.41$, but with comparatively smaller velocity fluctuations (i.e., $R_A < 1$). The positive cross helicity indicates propagation antiparallel to the magnetic field in the plasma frame (in this case also in the upstream direction, given the negative B_x).

The weaker cross helicity and smaller Alfvén ratio correspond with expectations for this frequency range. As the intrinsic frequency ω of the whistler mode wave increases above the proton cyclotron frequency Ω_i, both quantities should become smaller. For a parallel propagating whistler mode wave, one can show that the velocity fluctuation magnitude $\delta v = \frac{\Omega_i}{\Omega_i + \omega} v_{ph}$ (Gurnett & Bhattacharjee, 2017). Given the approximate whistler phase velocity $v_{ph} \cong v_A \sqrt{1 + \omega/\Omega_i}$ in this frequency range, we find that $\delta v \cong v_A \sqrt{\frac{\Omega_i}{\Omega_i + \omega}}$. Above the proton cyclotron frequency, therefore, both the cross helicity and Alfvén ratio should smoothly evolve toward zero with increasing frequency, as the ions become progressively less magnetized and respond less strongly to the wave. These properties therefore all appear consistent with an upstream-propagating whistler mode wave (thus, with right-handed intrinsic polarization) Doppler shifted by the solar wind flow, resulting in the observed left-handed polarization in the spacecraft frame.

We can also analyze the details of the phase-binned distribution functions. The distributions corresponding to the low-frequency wave identified in Figure 1 prove rather interesting. In Figure 5, we show cuts through velocity space distributions constructed from SWIA coarse data for each phase bin, as well as a phase-binned coarse energy spectrum, all of which show the presence of a number of different particle populations. The core solar wind proton population dominates the particle density, as usual. With the limited resolution of the coarse data, we see no obvious signatures of discrete populations of H^+ pickup ions at the expected locations in velocity space, in either the distribution cuts or the energy spectra. Even if such ions generate the waves, as seems very likely given the frequency, this process could occur upstream of the spacecraft. Alternatively, it could indicate that the waves have already scattered the pickup ions in phase space to form more broadly distributed populations.

Several other ion populations exist at higher energies. At twice the energy per charge of the protons (~1.5 keV/q), the solar wind alpha particle population shows no obvious modulation by the wave. Similarly, high-energy ions at ~8 keV/q (labeled "pickup" in Figure 5), consistent with O^+ and/or heavier pickup ions, do not obviously respond to the wave.

However, an ion population at energies of a few keV/q (labeled "non-SW" in Figure 5) does display clear variations with wave phase. The ions have a roughly constant velocity, with positive components along both the solar wind flow direction and the motional electric field direction. The origin of this population remains unclear, though it could potentially consist of either solar wind or pickup ions reflected from the bow shock. Though this population appears in the distribution for every phase bin, at approximately the same location in phase space, its density varies with wave phase. Intriguingly, the density of this population has a minimum when the wave electric field points toward its location in velocity space (i.e., phase bin 2) and a maximum when the wave electric field points opposite its location in velocity space (i.e., phase bin 6), potentially indicating a trapping mechanism. It is not antiphased with the solar wind proton velocity fluctuations, so it does not appear to represent the kind of momentum exchange postulated to occur in oscilliton-like structures (Dubinin et al., 2004).

Gyrophase-bunched ion populations have been observed previously in association with similar low-frequency waves in the terrestrial foreshock region (Fuselier et al., 1986; Mazelle et al., 2003; Thomsen et al., 1985), and their existence arises naturally for the right-hand resonant interaction likely at play in this case (Gary et al., 1986; Romanelli et al., 2018). However, the ions we observe do not appear to form a gyrating ring in phase space (at least not locally—other gyrophases must presumably appear at other locations). Instead, they appear at a relatively constant location in velocity space but with varying intensity in the spacecraft frame. We therefore suspect that these ions do not come from a population responsible for exciting the wave but instead merely respond to the wave's passage. This appears similar to the nonsolar-wind ions observed at the same time as a large-amplitude obliquely propagating magnetosonic wave previously analyzed at Mars (Ruhunusiri et al., 2016).

We speculate that the observed phase-dependent variations in this population may result from particle trapping in the low-frequency wave field. The relationship between the wave transverse electric field direction and the intensity of the bunched particles suggests that the transverse field may play a role. However, parallel electric fields associated with the slightly oblique propagation and/or nonlinearity of the wave could also potentially modulate these ions. Although these signatures present a rather intriguing subject for

future study, they are not the main focus of this manuscript. Instead, we proceed to test our technique on a larger sample of the MAVEN observations.

## 4. Properties of Plasma Waves Observed Upstream From Mars

We now proceed to apply our phase-binning technique to several months of MAVEN data. We pick two 3-month periods to test the methodology. The first period covers January, February, and March of 2018, a period of MAVEN solar wind coverage starting shortly after aphelion, during the southern winter and spring season. This period contains the observations shown in Figure 2. The second period covers September, October, and November of 2018, a period of MAVEN solar wind coverage surrounding perihelion, during the southern summer season. This period contains the observations shown in Figure 1.

For each of these time periods, we analyze all available MAG and SWIA data using exactly the same methodology as for our two test cases. We utilize 400-s intervals as our base unit of analysis. We advance the interval by 200 s at each step, so that we have 200 s overlap between each successive 400-s interval (for each UT day, we therefore analyze 431 separate intervals). For each such interval, we utilize the same procedures described above to compute phase-binned magnetic field and charged particle measurements for both the low-frequency and high-frequency ranges.

Since we wish to analyze only time periods which actually contain waves, we apply a number of criteria to select a meaningful subset of the results. We first apply selection criteria based on the eigenvalues from the minimum variance analysis of the filtered and detrended magnetic field data from each interval, by requiring $\frac{\lambda_{\max}}{\lambda_{\mathrm{int}}} < 2$ and $\frac{\lambda_{\mathrm{int}}}{\lambda_{\min}} > 4$. These loose criteria allow a substantial degree of both ellipticity and nonplanarity, as well as the possibility of errors in the estimation of the propagation dirction. However, a majority of the waves included in our analysis have greater circularity and planarity than these limits, and changing these limits does not greatly affect our subsequent conclusions. Together with the other constraints we apply, these values prove adequate for our purposes. We further require that the number of measurements accumulated in each of the eight phase bins does not differ by more than a factor of two, which restricts the nonlinearity of the waves.

We also require complete phase space coverage in each phase-binned velocity distribution, ensuring meaningful computations of the phase-binned moments. In order to eliminate measurements of nonwave magnetic field fluctuations in the ionosphere or magnetotail, we require $\beta_i > 0.01$ (using the ion thermal pressure computed from SWIA fine mode data). Finally, we require that $\frac{n_{\mathrm{coarse}}}{n_{\mathrm{fine}}} < 1.5$ and $\frac{\delta n_{\mathrm{fine}}/n_{\mathrm{fine}}}{\delta n_{\mathrm{coarse}}/n_{\mathrm{coarse}}} < 1.5$, as expressed in terms of the phase-binned density moments computed separately from SWIA coarse and fine mode data. These criteria ensure that the SWIA fine mode observations, which we utilize as the basis for most of the correlations and transport ratios we consider, contain the majority of the ion population. They also ensure that spurious oscillations from the solar wind moving into and out of the field of view do not affect our results. These final criteria, which could be relaxed in a future study, largely restrict the current analysis to the upstream solar wind.

We show a selection of the basic wave properties (Halekas, 2020) determined from our analysis in Figure 6, as a function of the background magnetic field direction and the observed frequency in the spacecraft frame. In the lower frequency range (left-hand column of Figure 6), we find that the great majority of the waves identified by our analysis have slightly elliptical left-handed polarizations and frequencies very close to the proton cyclotron frequency Ω_i in the spacecraft frame. Surprisingly, we note a small asymmetry in the observed frequencies, with slightly higher frequencies for antisunward magnetic fields than for sunward fields. We also see deviations from the proton cyclotron frequency, along with possible mode splitting, for magnetic fields nearly perpendicular to the solar wind flow. This likely results from the operation of a different instability mechanism, since for this perpendicular geometry, other modes can have higher growth rates than the usual right-hand resonant instability (Gary, 1991). We find that the waves in the proton cyclotron frequency band propagate within ~10–20° of the magnetic field direction, while the waves outside of this frequency range tend to have somewhat larger θ_{KB}. For most of the observed low-frequency waves, we observe clear and consistent cross helicity signatures. For the waves near and above the proton cyclotron frequency,
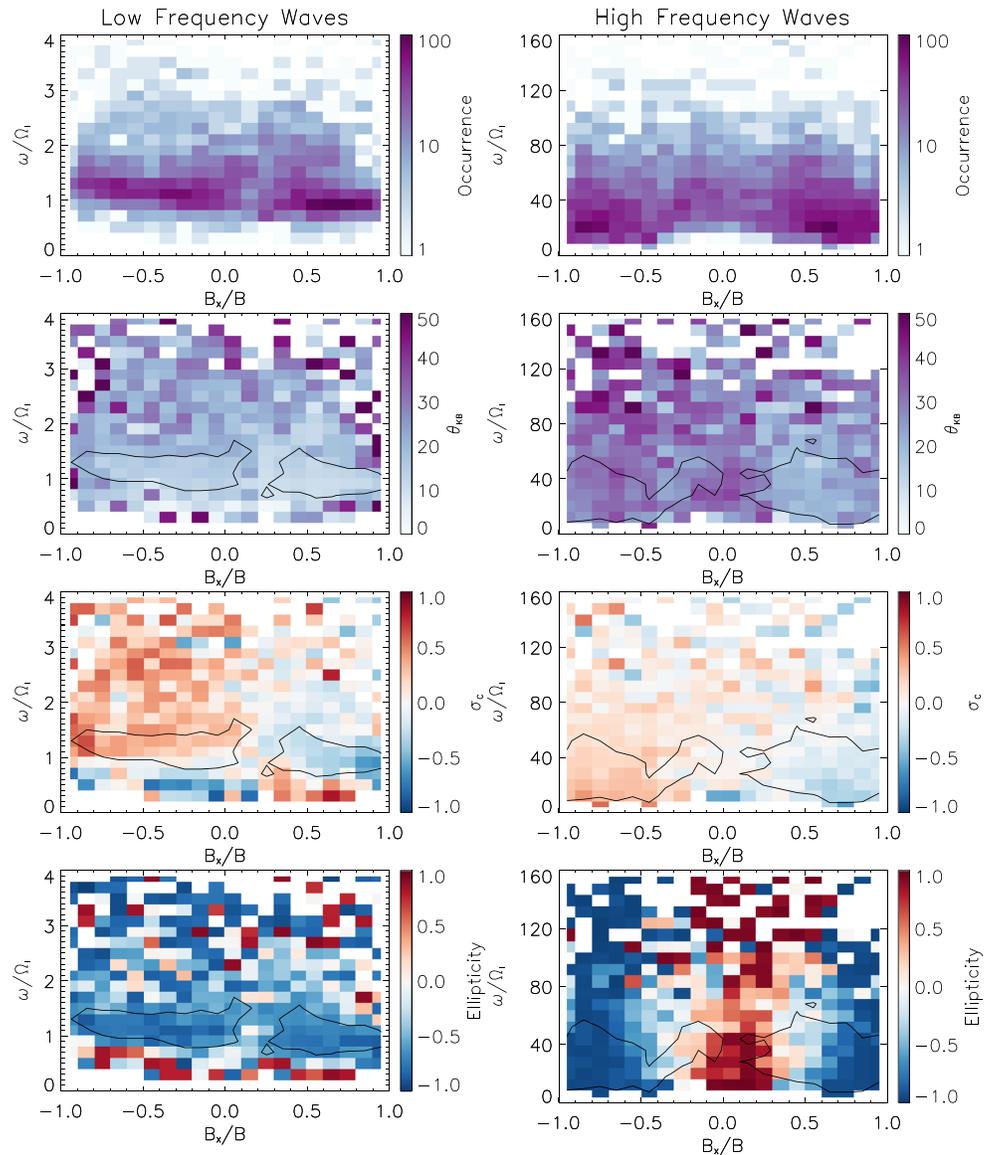
Figure 6. Selected wave parameters for low-frequency (left column) and high-frequency (right column) waves, as a function of the normalized MSO x component of the background magnetic field B_x/B_0 (i.e., the cosine of the cone angle) and the normalized spacecraft frame wave frequency ω/Ω_i. The top row shows the wave occurrence (the number of analysis intervals with the wave parameters in question) as a function of these parameters. The second row shows the average wave normal angle θ_{KB} between the propagation direction and the magnetic field, arbitrarily referenced to 0–90° to deal with the 180° ambiguity from minimum variance analysis. The third row shows the average cross helicity σ_c, with negative values indicating propagation parallel to the magnetic field, and positive values indicating antiparallel propagation. The bottom row shows the average ellipticity from minimum variance analysis (negative values indicate left-handed wave rotation around the magnetic field in the spacecraft frame; positive values indicate right-handed rotation). Contours outline the range of the most commonly observed wave parameters.

we find positive cross helicities for antisunward fields and negative cross helicities for sunward fields, clearly indicating predominantly upstream propagation in the plasma frame.

Given the corresponding left-handed polarization values, these results suggest that the great majority of the waves in the lower frequency range propagate upstream with intrinsic right-handed polarization, with the Doppler shift of the solar wind flow sweeping them downstream and reversing the sign of their polarization in the spacecraft frame. These properties all appear consistent with the fast magnetosonic mode, consistent with the conclusions of previous studies (Romanelli et al., 2013).
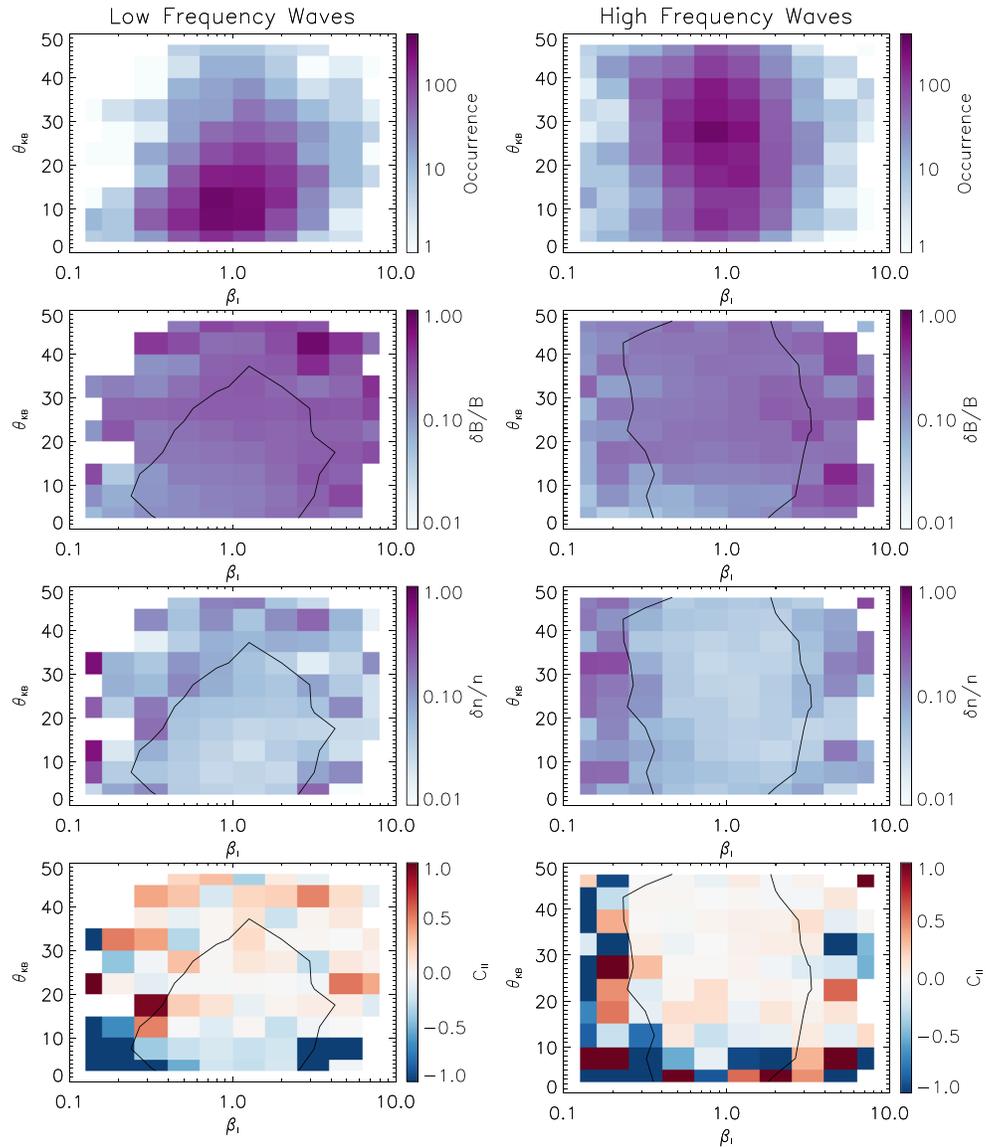
Figure 7. Selected wave parameters for low-frequency (left column) and high-frequency (right column) waves, as a function of the ratio of the proton thermal pressure to magnetic pressure β_i and the angle θ_{KB} between the propagation direction and the magnetic field. The top row shows the wave occurrence (the number of analysis intervals with the wave parameters in question) as a function of these parameters. The second and third rows show the average RMS amplitudes of the magnetic field and density fluctuations $\delta B/B_0$ and $\delta n/n_0$. The bottom panel shows the average parallel compressibility $C_{||}$, with positive values indicating in-phase compressional magnetic field and density fluctuations and negative values indicating out-of-phase fluctuations. Contours outline the range of the most commonly observed wave parameters.

A small population of waves with spacecraft frame frequencies below the proton cyclotron frequency has right-handed polarization in the spacecraft frame and cross helicity values that indicate downstream propagation. This population of waves could result from a nonresonant interaction with pickup H^+ or with protons reflected from the bow shock (Gary et al., 1984).

In the higher frequency range (right-hand column of Figure 6), we observe a much broader range of polarizations and frequencies in the spacecraft frame. The waves identified by our analysis have spacecraft frame frequencies up to ~120 Ω_i, with a slight trend toward higher frequencies for more perpendicular background fields. They propagate at oblique angles of ~15–45° from the magnetic field. Again, we note a surprising and

unexplained asymmetry, with slightly larger average θ_{KB} values for antisunward fields and smaller θ_{KB} values for sunward fields. For spacecraft frame frequencies up to ~60 Ω_i, we find cross helicity signatures fairly similar to those in the lower frequency range, with positive values for antisunward fields and negative values for sunward fields, again indicating prevailing upstream propagation. The observed cross helicities decrease in magnitude with increasing frequency, consistent with the theoretical expectations for whistler mode waves discussed in section 3.

The observed spacecraft frame polarizations in the higher frequency range vary strongly with the magnetic field direction, with near-circular left-handed polarizations for sunward and antisunward fields, near-circular right-handed polarizations for fields perpendicular to the sunward direction, and a mixed signal at intermediate field angles. This agrees with previous studies (Brain et al., 2002; Ruhunusiri et al., 2018) and supports an identification of whistler mode waves. These polarization trends result from the larger Doppler shift of waves traveling antiparallel/parallel to the field for sunward/antisunward background fields. The trend toward higher observed spacecraft frame frequencies for perpendicular fields (and thus right-handed polarization) agrees with terrestrial observations (Fairfield, 1974) and likely also results from the effects of the Doppler shift.

We next show a selection of results from our analysis related to the compressibility of the waves in Figure 7, as a function of β_i and the wave normal angle θ_{KB}. We choose these specific organizing parameters for ease of comparison with theoretical results (Gary & Winske, 1992; Krauss-Varban et al., 1994). However, we emphasize that the theoretical predictions in the literature are typically shown for fixed values of some parameters (e.g., the wavenumber), whereas our results have variations in all parameters.

In the lower frequency range (left column of Figure 7), we find that the majority of the waves identified by our analysis propagate in a background plasma with moderate β_i values (most within a factor of three of unity), completely consistent with the average properties of the solar wind at Mars (Halekas et al., 2017). We note a weak trend of lower θ_{KB} during low β_i conditions and higher θ_{KB} during high β_i conditions. This could result from the damping of parallel propagating fast mode waves in high β_i conditions (Gary & Winske, 1992). We also find variations in both the magnetic field and density fluctuation amplitudes. The fractional magnetic field fluctuation amplitudes increase with both β_i and θ_{KB}. The fractional density fluctuation amplitudes, on other hand, also increase with θ_{KB} but do not vary as clearly with β_i. The compressibility C_{Bn} formed from the ratio of these two fluctuating amplitudes (not shown) therefore decreases with β_i but varies only weakly with θ_{KB}. This does not obviously agree with theoretical expectations for the fast mode (Krauss-Varban et al., 1994), which predict a compressibility that decreases with β_i but increases strongly with θ_{KB} at small values. This may indicate that the observations could include some admixture of slow or mirror mode waves, which have very large compressibility at small values of θ_{KB}, though neither is theoretically expected. However, it could instead indicate variations in the wavenumber or some other parameter that affects the compressibility.

Meanwhile, from the density and magnetic field magnitude fluctuations and their phases, we find small positive parallel compressibilities over most of parameter space for the lower frequency range, indicating correlated fluctuations, consistent with previous observations (Mazelle et al., 2004; Romanelli et al., 2013). The $C_{||}$ values do not clearly vary with β_i but do decrease at small values of θ_{KB}. In fact, we find evidence for small negative average $C_{||}$ values (indicating slightly anticorrelated density and magnetic field fluctuations) for the smallest values of θ_{KB}. This appears consistent with theoretical expectations for moderate to high β_i conditions but not with those for low β_i (Krauss-Varban et al., 1994). The apparent discrepancies at low β_i could again point to some admixture of slow modes at small values of θ_{KB}.

In the higher frequency range (right column of Figure 7), we again find that the majority of waves identified by our analysis propagate in a background plasma with moderate β_i values; however, in this case, we find no correlation between β_i and θ_{KB}. The fractional magnetic field fluctuation amplitudes again increase with both β_i and θ_{KB}. The fractional density fluctuation amplitudes, on other hand, have small values at intermediate β_i but larger values at both low and high β_i, with the larger amplitudes appearing primarily in the least populated regions of parameter space. We do not expect significant density fluctuations for waves in this frequency range. If these values are accurate, they might indicate some nonlinearity. In any case,
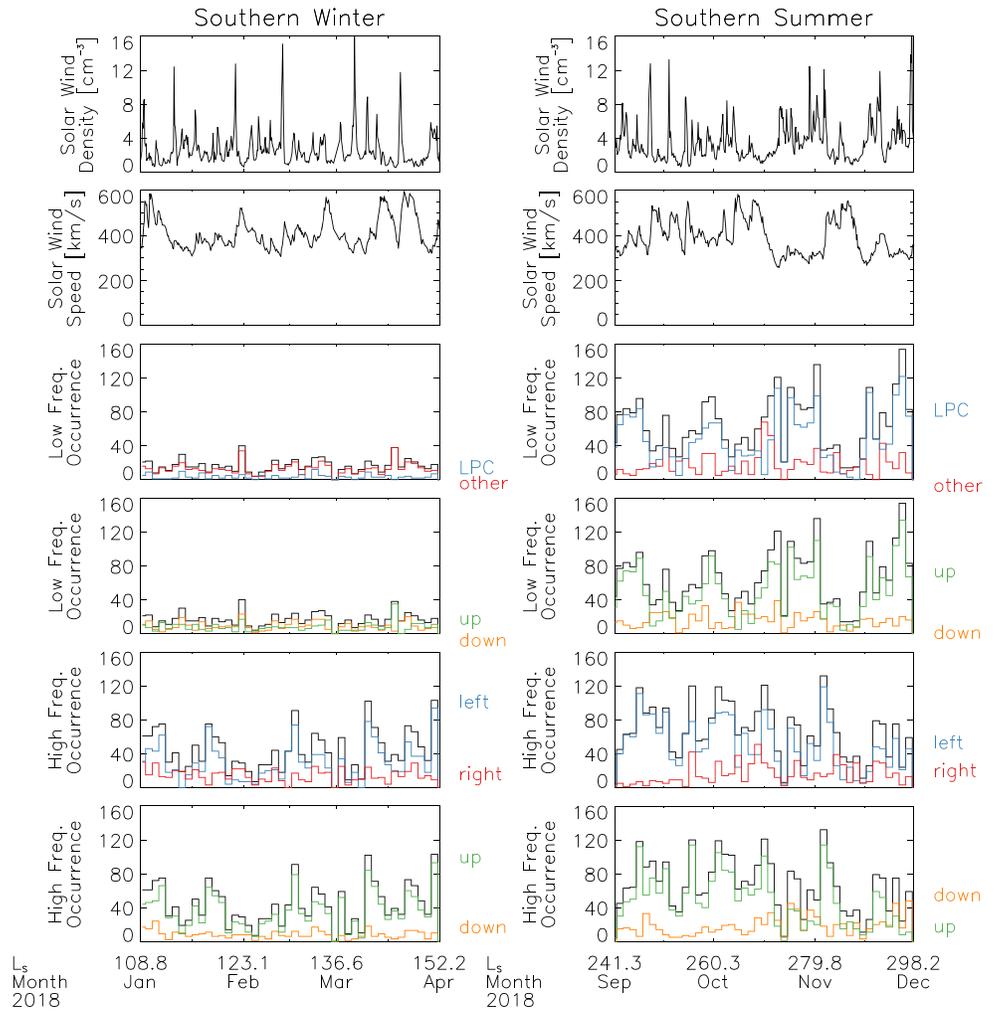
Figure 8. Temporal occurrence (the number of analysis intervals with waves identified) of waves of different types for the two time periods analyzed, a 3-month period near southern winter and aphelion in the left column and a 3-month period near southern summer and perihelion in the right column. For context, the top two panels show the upstream solar wind density and speed. The third panel shows the occurrence (per 2-day period) of low-frequency waves with frequencies near the proton cyclotron frequency Ω_i and left-handed polarization in the spacecraft frame, as compared to all other low-frequency waves. The fourth panel shows the occurrence of low-frequency waves propagating upstream and downstream in the plasma frame, as determined from the cross helicity. The fifth panel shows the occurrence of high-frequency waves with left-handed and right-handed polarization in the spacecraft frame. The sixth panel shows the occurrence of high-frequency waves propagating upstream and downstream in the plasma frame.

these fluctuations result in compressibility values (not shown) that decrease with both β_i and θ_{KB}, also not obviously consistent with theoretical expectations for the whistler mode.

Meanwhile, the parallel compressibilities for the higher frequency range, though rather noisy, have values near zero over most of parameter space, as expected for this frequency range. We find $C_{\parallel}$ values with large magnitudes but mixed signs at the lowest and highest values of β_i and at low values of θ_{KB}. However, we note that the large magnitudes of $C_{\parallel}$ for low β_i and low θ_{KB} likely result at least in part from very small values of the ratio $\dfrac{\langle \delta B_{\parallel} \cdot \delta B_{\parallel} \rangle}{\langle B_0{}^2 \rangle}$ that appear in the denominator of $C_{\parallel}$, which amplify any noise present in the density fluctuations. Therefore, we draw no strong conclusions from these observations.

We next consider the temporal occurrence (i.e., the number of analysis intervals with waves identified) of the waves identified by our analysis, over the two 3-month time periods we analyzed, as shown in Figure 8. For
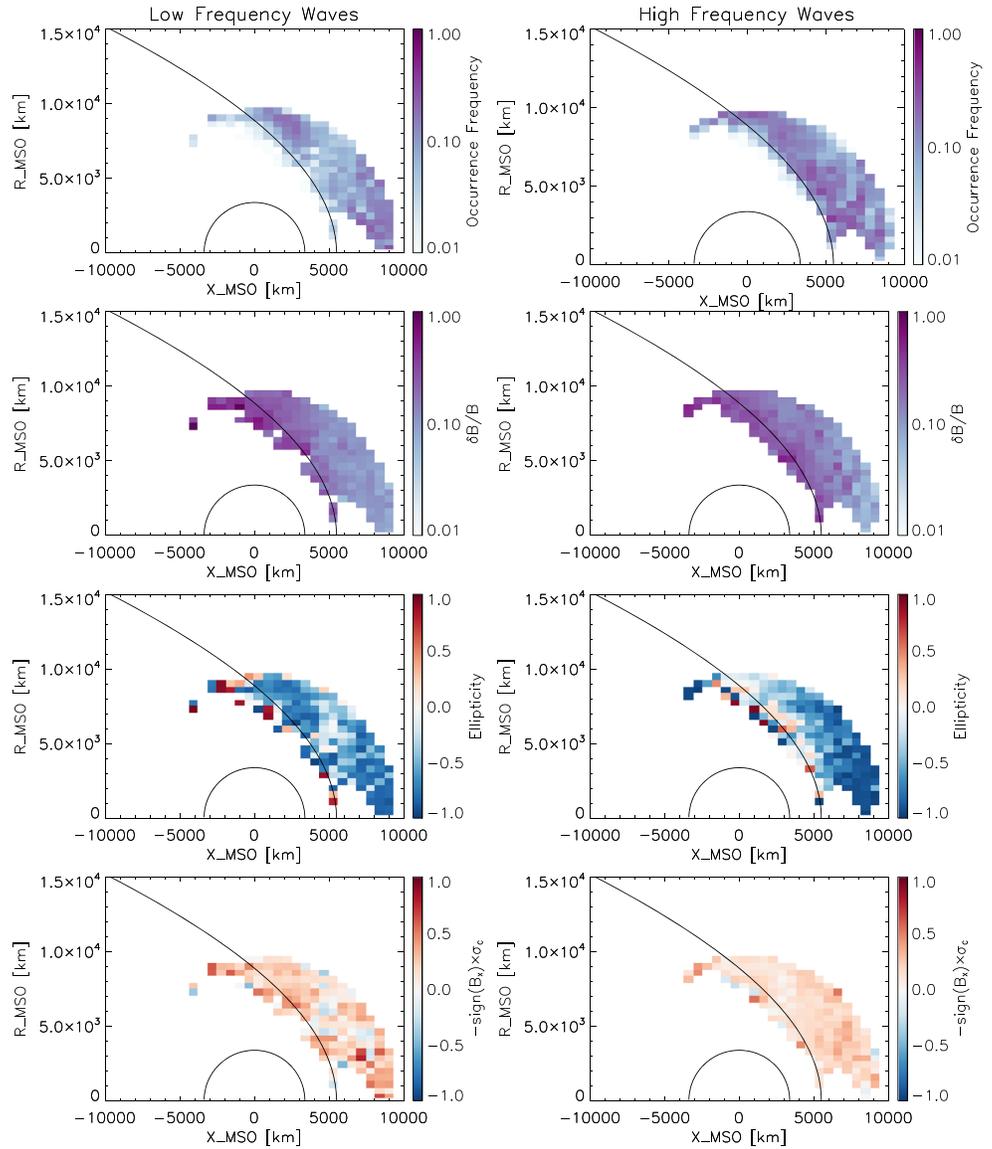
Figure 9. Spatial distributions of selected wave parameters for low-frequency (left column) and high-frequency (right columns) waves in cylindrical MSO coordinates. The top row shows the spatial occurrence frequency of these waves (the fraction of analysis intervals with waves). The second row shows the RMS amplitude of the magnetic field fluctuations $\delta\mathbf{B}/B_0$. The third row shows the wave ellipticity, with positive values indicating right-handed polarization in the spacecraft frame and negative values indicating left-handed polarization. The fourth panel shows the cross helicity multiplied by the opposite of the sign of B_x, such that positive values indicate waves propagating upstream in the plasma frame, and negative values indicate waves propagating downstream in the plasma frame. The conic section curve indicates the nominal bow shock position (Trotignon et al., 2006).

waves in both frequency ranges, the total occurrence reaches ~120 analysis intervals per 2-day period. This represents a ~14% occurrence frequency (i.e., the number of analysis intervals with waves identified divided by the total number of analysis intervals) for the entire orbit, but closer to ~30% in the solar wind, given that MAVEN spends only ~50% of its orbit in the solar wind during these intervals.

For the lower frequency waves (middle panels of Figure 8), we compare the properties of waves with left-handed polarization and frequencies near the proton cyclotron frequency (0.7–1.5 Ω_i) in the spacecraft frame to all other waves identified by our analysis. We find that the occurrence of the proton cyclotron frequency band waves increases by over an order of magnitude during the southern summer season, consistent

with previous results (Bertucci et al., 2013; Romanelli et al., 2013, 2016). On the other hand, the occurrence of the out of band waves varies only slightly, with at most a small increase in southern summer. Some fraction of these out of band waves might result from the nonlinear evolution of waves in the proton cyclotron frequency band, which could explain a small increase in occurrence in southern summer. In southern winter, the proton cyclotron frequency band waves occur less frequently than the out of band waves, while in southern summer, they occur more frequently. Meanwhile, we find a much higher rate of occurrence of waves propagating upstream in the plasma frame (as determined from cross helicity values) during southern summer but an almost equal rate of upstream and downstream propagation directions in southern winter. Unexpectedly, during the southern summer season we find a much larger rate of occurrence of both upstream-propagating and left-hand polarized waves in the proton cyclotron frequency band during high-density and low-speed solar wind conditions. We are unaware of a previous report of such a trend at Mars. However, a similar trend with solar wind speed exists at Venus, and it may arise from the longer solar wind transit time across the exosphere, which allows greater time for wave growth (Delva et al., 2015).

For the higher frequency waves (bottom panels of Figure 8), we find a higher occurrence of waves with left-handed polarization in the spacecraft frame and a higher occurrence of waves propagating upstream in the plasma frame, with similar fractions in both two time periods. The total occurrence of the higher frequency waves increases by less than a factor of two in the southern summer, appreciable but not nearly as large as the increase for the lower frequency waves. We find no significant correlation between the overall occurrence of lower and higher frequency waves during either individual time period, with linear correlation coefficients of ~0.3 and ~0.05 between the occurrence in the southern winter and summer periods, respectively. We also find no significantly higher correlations between any of the different classes of lower and higher frequency waves, consistent with the results of previous studies (Brain et al., 2002).

As a final exercise, we map the spatial occurrence of the waves identified by our analysis in cylindrical coordinates around Mars, as shown in Figure 9. Both lower and higher frequency waves can occur close to the nominal bow shock position or anywhere upstream, with similar occurrence frequency throughout the upstream region sampled by MAVEN during this time. The apparent spatial variations in the occurrence of the lower frequency waves largely result from the differences in the orbit between the southern winter and summer time periods we analyzed, which have dramatically different wave occurrence rates.

Waves in both frequency ranges have higher amplitudes near the bow shock than upstream. The amplitude of the higher frequency waves falls off slightly more rapidly with distance from the bow shock, likely reflecting the different wave generation locations and instability mechanisms. The lower frequency waves have predominantly left-handed polarization in the spacecraft frame everywhere. The higher frequency waves, on the other hand, have predominantly left-handed polarization in the spacecraft frame over most of the upstream region, but mixed or even slightly right-handed average polarization near the nominal bow shock location. This may reflect a different generation mechanism operating near the shock, or a propagation effect. Finally, waves in both frequency ranges have predominantly upstream average propagation in the plasma frame. Given the similar relative rates of upstream and downstream propagating waves in the two frequency ranges shown in Figure 8, the smaller average cross helicities of the higher frequency waves must primarily reflect the expected decrease in ion velocity fluctuation magnitude with increasing wave frequency discussed in section 3.

5. Conclusions

The results described in this manuscript serve in part to introduce and validate a new technique for increasing the frequency range of plasma waves that we can analyze through the use of correlations and transport ratios. These results show that by subsampling and binning the charged particle velocity distribution measurements by the wave phase, we can analyze the relationship between magnetic field and charged particle measurements in a frequency range previously inaccessible at Mars. While we can only apply this technique to the subset of plasma waves that remains nearly coherent over multiple wave periods, we have shown that we can fruitfully utilize it to analyze two important classes of waves observed upstream from Mars. In addition to proving the applicability of the technique, our analysis reveals a number of interesting scientific results, some of which deserve further study.

Cross helicity values for both waves near the proton cyclotron frequency and higher frequency whistler mode waves indicate that the great majority of these waves propagate upstream in the plasma frame. This supports the conclusions of most previous studies of these two classes of waves but allows a clearer determination of their intrinsic mode and properties. These results also enable more detailed analysis of the propagation of the plasma waves in any given individual observation, whereas many previous studies could only draw statistical conclusions based on many observations. As a result, we can investigate both the temporal and spatial variation in the occurrence of waves with a given propagation direction.

The predominant characteristics of observed waves in the lower frequency range have little spatial variability but do have large temporal variations. The occurrence of upstream-propagating waves with spacecraft frame frequencies equal to the proton cyclotron frequency varies strongly with season, almost certainly due to the seasonal changes in the hydrogen exosphere. The upstream propagation direction inferred from cross helicity values supports the identification of these waves as intrinsically right-handed fast magnetosonic mode waves, Doppler shifted to left-handed polarization in the spacecraft frame.

In contrast, the predominant characteristics of waves in the higher frequency range have less temporal variability but some spatial variability. These waves have a predominant upstream propagation at all locations, but a polarization in the spacecraft frame that varies both with magnetic field direction and with location, with more right-handed polarization observed for magnetic fields perpendicular to the flow and at locations near the nominal bow shock location. The former trend agrees with previous results and with expectations for whistler mode waves, but the latter trend may deserve more study.

We also find several indications of the presence of multiple wave modes in the lower frequency wave observations. The waves propagating nearly along the background magnetic field have rather different compressibility values than those propagating at even slightly oblique angles. The field-aligned waves have unexpectedly large compressibilities as well as negative parallel compressibilities corresponding to anticorrelated density and magnetic field variations. Together, these results may indicate the admixture of some slow magnetosonic mode waves. A small occurrence of downstream propagating waves with right-handed polarization and frequencies below the proton cyclotron frequency in the spacecraft frame suggests the presence of a nonresonant mode. Finally, an apparent signature of mode splitting for magnetic fields perpendicular to the solar wind flow may indicate yet another mode, consistent with the different predominant instabilities expected to operate in this geometry.

The results discussed in this paper only scratch the surface of the potential applications of this technique. In principle, one could apply the technique to more nonlinear waves, less planar waves, or even linearly polarized waves, given an appropriate definition for wave phase. The analysis of phase-dependent ion populations, potentially including gyrophase-bunched ions, deserves more attention. And, of course, one could also utilize similar techniques to analyze the electron properties during the occurrence of plasma waves.

Data Availability Statement

All MAVEN data and ephemerides used in this study are available from the Planetary Data System (https://pds-ppi.igpp.ucla.edu/mission/MAVEN). A data set containing the times of and parameters computed for the plasma wave observations discussed in this study is archived and publicly available (Halekas, 2020).

References

Anderson, J., Donald, E., & Hord, C. W. (1971). Mariner 6 and 7 ultraviolet spectrometer experiment: Analysis of hydrogen Lyman-alpha data. *Journal of Geophysical Research*, *76*(28), 6666–6673. https://doi.org/10.1029/JA076i028p06666

Barnes, A. (1970). Theory of generation of bow-shock-associated hydromagnetic waves in the upstream interplanetary medium. *Cosmic Electrodynamics*, *1*, 90–114.

Bertucci, C., Romanelli, N., Chaufray, J. Y., Gomez, D., Mazelle, C., Delva, M., et al. (2013). Temporal variability of waves at the proton cyclotron frequency upstream from Mars: Implications for Mars distant hydrogen exosphere. *Geophysical Research Letters*, *40*, 3809–3813. https://doi.org/10.1002/grl.50709

Bhattacharyya, D., Clarke, J. T., Bertaux, J.-L., Chaufray, J.-Y., & Mayyasi, M. (2015). A strong seasonal dependence in the Martian hydrogen exosphere. *Geophysical Research Letters*, *42*, 8678–8685. https://doi.org/10.1002/2015GL065804

Brain, D. A., Bagenal, F., Acuña, M. H., Connerney, J. E. P., Crider, D. H., Mazelle, C., et al. (2002). Observations of low-frequency electromagnetic plasma waves upstream from the Martian shock. *Journal of Geophysical Research*, *107*(A6), 1076. https://doi.org/10.1029/2000JA000416

Brinca, A. L. (1991). Cometary linear instabilities: From profusion to perspective. In *Cometary plasma processes* (pp. 211–221). Washington, DC: American Geophysical Union. https://doi.org/10.1029/GM061p0211

Chaffin, M. S., Chaufray, J.-Y., Stewart, I., Montmessin, F., Schneider, N. M., & Bertaux, J.-L. (2014). Unexpected variability of Martian hydrogen escape. *Geophysical Research Letters*, *41*, 314–320. https://doi.org/10.1002/2013GL058578

Connerney, J. E. P., Espley, J., Lawton, P., Murphy, S., Odom, J., Oliversen, R., & Sheppard, D. (2015). The MAVEN magnetic field investigation. *Space Science Reviews*, *195*(1–4), 257–291. https://doi.org/10.1007/s11214-015-0169-4

Delva, M., Bertucci, C., Volwerk, M., Lundin, R., Mazelle, C., & Romanelli, N. (2015). Upstream proton cyclotron waves at Venus near solar maximum. *Journal of Geophysical Research: Space Physics*, *120*, 344–354. https://doi.org/10.1002/2014JA020318

Delva, M., Mazelle, C., & Bertucci, C. (2011). Upstream ion cyclotron waves at Venus and Mars. *Space Science Reviews*, *162*(1-4), 5–24. https://doi.org/10.1007/s11214-011-9828-2

Delva, M., Zhang, T. L., Volwerk, M., Magnes, W., Russell, C. T., & Wei, H. Y. (2008). First upstream proton cyclotron wave observations at Venus. *Geophysical Research Letters*, *35*, L03105. https://doi.org/10.1029/2007GL032594

Dubinin, E., & Fraenz, M. (2016). Ultra-low-frequency waves at Venus and Mars. In *Low-frequency waves in space plasmas* (pp. 343–364). Washington, DC: American Geophysical Union. https://doi.org/10.1002/9781119055006.ch20

Dubinin, E., Fraenz, M., Woch, J., Barabash, S., Lundin, R., & Yamauchi, M. (2006). Hydrogen exosphere at Mars: Pickup protons and their acceleration at the bow shock. *Geophysical Research Letters*, *33*, L22103. https://doi.org/10.1029/2006GL027799

Dubinin, E., Fränz, M., Woch, J., Roussos, E., Barabash, S., Lundin, R., et al. (2006). Plasma morphology at Mars. ASPERA-3 observations. *Space Science Reviews*, *126*(1–4), 209–238. https://doi.org/10.1007/s11214-006-9039-4

Dubinin, E., Sauer, K., & McKenzie, J. F. (2004). Nonlinear stationary waves and solitons in ion beam-plasma configuration. *Journal of Geophysical Research*, *109*, A02208. https://doi.org/10.1029/2003JA010283

Eastwood, J. P., Balogh, A., Dunlop, M. W., Horbury, T. S., & Dandouras, I. (2002). Cluster observations of fast magnetosonic waves in the terrestrial foreshock. *Geophysical Research Letters*, *29*, 2046. https://doi.org/10.1029/2002GL015582

Eastwood, J. P., Balogh, A., Mazelle, C., Dandouras, I., & Rème, H. (2004). Oblique propagation of 30 s period fast magnetosonic foreshock waves: A Cluster case study. *Geophysical Research Letters*, *31*, L04804. https://doi.org/10.1029/2003GL018897

Eastwood, J. P., Lucek, E. A., Mazelle, C., Meziane, K., Narita, Y., Pickett, J., & Treumann, R. A. (2005). The foreshock. *Space Science Reviews*, *118*(1–4), 41–94. https://doi.org/10.1007/s11214-005-3824-3

Fairfield, D. H. (1969). Bow shock associated waves observed in the far upstream interplanetary medium. *Journal of Geophysical Research*, *74*(14), 3541–3553. https://doi.org/10.1029/JA074i014p03541

Fairfield, D. H. (1974). Whistler waves observed upstream from collisionless shocks. *Journal of Geophysical Research*, *79*(10), 1368–1378. https://doi.org/10.1029/JA079i010p01368

Feldman, P. D., Steffl, A. J., Parker, J. W., A'Hearn, M. F., Bertaux, J.-L., Alan Stern, S., et al. (2011). Rosetta-Alice observations of exospheric hydrogen and oxygen on Mars. *Icarus*, *214*(2), 394–399. https://doi.org/10.1016/j.icarus.2011.06.013

Fuselier, S. A., Thomsen, M. F., Gary, S. P., Bame, S. J., Russell, C. T., & Parks, G. K. (1986). The phase relationship between gyrophase-bunched ions and MHD-like waves. *Geophysical Research Letters*, *13*(1), 60–63. https://doi.org/10.1029/GL013i001p00060

Gary, S. P. (1991). Electromagnetic ion/ion instabilities and their consequences in space plasmas: A review. *Space Science Reviews*, *56*(3-4), 373–415. https://doi.org/10.1007/BF00196632

Gary, S. P., Gosling, J. T., & Forslund, D. W. (1981). The electromagnetic ion beam instability upstream of the Earth's bow shock. *Journal of Geophysical Research*, *86*(A8), 6691–6696. https://doi.org/10.1029/JA086iA08p06691

Gary, S. P., Smith, C. W., Lee, M. A., Goldstein, M. L., & Forslund, D. W. (1984). Electromagnetic ion beam instabilities. *The Physics of Fluids*, *27*(7), 1852–1862. https://doi.org/10.1063/1.864797

Gary, S. P., Thomsen, M. F., & Fuselier, S. A. (1986). Electromagnetic instabilities and gyrophase-bunched particles. *The Physics of Fluids*, *29*(2), 531–535. https://doi.org/10.1063/1.865441

Gary, S. P., & Winske, D. (1992). Correlation function ratios and the identification of space plasma instabilities. *Journal of Geophysical Research*, *97*(A3), 3103–3111. https://doi.org/10.1029/91JA02752

Gurnett, D. A., & Bhattacharjee, A. (2017). *Introduction to plasma physics: With space, laboratory and astrophysical applications* (2nd ed.). Cambridge: Cambridge University Press. Retrieved from. https://www.cambridge.org/core/books/introduction-to-plasma-physics/8AEBEABFE6F0E5759FE0D92820ED6DF5, https://doi.org/10.1017/9781139226059

Halekas, J. S. (2017). Seasonal variability of the hydrogen exosphere of Mars. *Journal of Geophysical Research: Planets*, *122*, 901–911. https://doi.org/10.1002/2017JE005306

Halekas, J. S. (2020). Transport ratios for plasma waves observed by MAVEN at Mars [data set]. Zenodo. https://doi.org/10.5281/zenodo.3820237

Halekas, J. S., McFadden, J. P., Connerney, J. E. P., Espley, J. R., Brain, D. A., Mitchell, D. L., et al. (2015). Time-dispersed ion signatures observed in the Martian magnetosphere by MAVEN. *Geophysical Research Letters*, *42*, 8910–8916. https://doi.org/10.1002/2015GL064781

Halekas, J. S., Ruhunusiri, S., Harada, Y., Collinson, G., Mitchell, D. L., Mazelle, C., et al. (2017). Structure, dynamics, and seasonal variability of the Mars-solar wind interaction: MAVEN solar wind ion analyzer in-flight performance and science results. *Journal of Geophysical Research: Space Physics*, *122*, 547–578. https://doi.org/10.1002/2016JA023167

Halekas, J. S., Taylor, E. R., Dalton, G., Johnson, G., Curtis, D. W., McFadden, J. P., et al. (2015). The solar wind ion analyzer for MAVEN. *Space Science Reviews*, *195*(1–4), 125–151. https://doi.org/10.1007/s11214-013-0029-z

Hoppe, M. M., & Russell, C. T. (1983). Plasma rest frame frequencies and polarizations of the low-frequency upstream waves: ISEE 1 and 2 observations. *Journal of Geophysical Research*, *88*(A3), 2021–2027. https://doi.org/10.1029/JA088iA03p02021

Jakosky, B. M., Lin, R. P., Grebowsky, J. M., Luhmann, J. G., Mitchell, D. F., Beutelschies, G., et al. (2015). The Mars Atmosphere and Volatile Evolution (MAVEN) mission. *Space Science Reviews*, *195*(1–4), 3–48. https://doi.org/10.1007/s11214-015-0139-x

Jian, L. K., Wei, H. Y., Russell, C. T., Luhmann, J. G., Klecker, B., Omidi, N., et al. (2014). Electromagnetic waves near the proton cyclotron frequency: STEREO observations. *The Astrophysical Journal*, *786*(2), 123. https://doi.org/10.1088/0004-637X/786/2/123

Krauss-Varban, D., Omidi, N., & Quest, K. B. (1994). Mode properties of low-frequency waves: Kinetic theory versus Hall-MHD. *Journal of Geophysical Research*, *99*(A4), 5987–6009. https://doi.org/10.1029/93JA03202

Le, G., & Russell, C. T. (1994). The morphology of ULF waves in the Earth's foreshock. In *Solar wind sources of magnetospheric ultra-low-frequency waves* (pp. 87–98). Washington, DC: American Geophysical Union. https://doi.org/10.1029/GM081p0087

Le, G., Chi, P. J., Blanco-Cano, X., Boardsen, S., Slavin, J. A., Anderson, B. J., & Korth, H. (2013). Upstream ultra-low frequency waves in Mercury's foreshock region: MESSENGER magnetic field observations. *Journal of Geophysical Research: Space Physics*, *118*, 2809–2823. https://doi.org/10.1002/jgra.50342

Lee, M. A. (1989). Ultra-low frequency waves at comets. In *Plasma waves and instabilities at comets and in magnetospheres* (pp. 13–29). Washington, DC: American Geophysical Union. https://doi.org/10.1029/GM053p0013

Matthaeus, W. H., & Goldstein, M. L. (1982). Measurement of the rugged invariants of magnetohydrodynamic turbulence in the solar wind. *Journal of Geophysical Research*, *87*(A8), 6011–6028. https://doi.org/10.1029/JA087iA08p06011

Mazelle, C., Meziane, K., LeQuéau, D., Wilber, M., Eastwood, J. P., Rème, H., et al. (2003). Production of gyrating ions from nonlinear wave–particle interaction upstream from the Earth's bow shock: A case study from Cluster-CIS. *Planetary and Space Science*, *51*(12), 785–795. https://doi.org/10.1016/j.pss.2003.05.002

Mazelle, C., & Neubauer, F. M. (1993). Discrete wave packets at the proton cyclotron frequency at comet P/Halley. *Geophysical Research Letters*, *20*(2), 153–156. https://doi.org/10.1029/92GL02613

Mazelle, C., Winterhalter, D., Sauer, K., Trotignon, J. G., Acuña, M. H., Baumgärtel, K., et al. (2004). Bow shock and upstream phenomena at Mars. *Space Science Reviews*, *111*(1/2), 115–181. https://doi.org/10.1023/B:SPAC.0000032717.98679.d0

Nagy, A. F., Winterhalter, D., Sauer, K., Cravens, T. E., Brecht, S., Mazelle, C., et al. (2004). The plasma environment of Mars. *Space Science Reviews*, *111*(1/2), 33–114. https://doi.org/10.1023/B:SPAC.0000032718.47512.92

Orlowski, D. S., Crawford, G. K., & Russell, C. R. (1990). Upstream waves at Mercury, Venus and Earth: Comparison of the properties of one hertz waves. *Geophysical Research Letters*, *17*(13), 2293–2296. https://doi.org/10.1029/GL017i013p02293

Orlowski, D. S., Russell, C. T., & Lepping, R. P. (1992). Wave phenomena in the upstream region of Saturn. *Journal of Geophysical Research*, *97*(A12), 19,187–19,199. https://doi.org/10.1029/92JA01461

Rahmati, A., Larson, D. E., Cravens, T. E., Lillis, R. J., Halekas, J. S., McFadden, J. P., et al. (2017). MAVEN measured oxygen and hydrogen pickup ions: Probing the Martian exosphere and neutral escape. *Journal of Geophysical Research: Space Physics*, *122*, 3689–3706. https://doi.org/10.1002/2016JA023371

Rahmati, A., Larson, D. E., Cravens, T. E., Lillis, R. J., Halekas, J. S., McFadden, J. P., et al. (2018). Seasonal variability of neutral escape from Mars as derived from MAVEN pickup ion observations. *Journal of Geophysical Research: Planets*, *123*, 1192–1202. https://doi.org/10.1029/2018JE005560

Romanelli, N., Bertucci, C., Gómez, D., Mazelle, C., & Delva, M. (2013). Proton cyclotron waves upstream from Mars: Observations from Mars Global Surveyor. *Planetary and Space Science*, *76*, 1–9. https://doi.org/10.1016/j.pss.2012.10.011

Romanelli, N., DiBraccio, G., Gershman, D., le, G., Mazelle, C., Meziane, K., et al. (2020). Upstream ultra-low frequency waves observed by MESSENGER's magnetometer: Implications for particle acceleration at Mercury's bow shock. *Geophysical Research Letters*, *47*, e2020GL087350. https://doi.org/10.1029/2020GL087350

Romanelli, N., Mazelle, C., Chaufray, J. Y., Meziane, K., Shan, L., Ruhunusiri, S., et al. (2016). Proton cyclotron waves occurrence rate upstream from Mars observed by MAVEN: Associated variability of the Martian upper atmosphere. *Journal of Geophysical Research: Space Physics*, *121*, 11,113–11,128. https://doi.org/10.1002/2016JA023270

Romanelli, N., Mazelle, C., & Meziane, K. (2018). Nonlinear wave-particle interaction: Implications for newborn planetary and back-streaming proton velocity distribution functions. *Journal of Geophysical Research: Space Physics*, *123*, 1100–1117. https://doi.org/10.1002/2017JA024691

Ruhunusiri, S., Halekas, J. S., Connerney, J. E. P., Espley, J. R., McFadden, J. P., Larson, D. E., et al. (2015). Low-frequency waves in the Martian magnetosphere and their response to upstream solar wind driving conditions. *Geophysical Research Letters*, *42*, 8917–8924. https://doi.org/10.1002/2015GL064968/

Ruhunusiri, S., Halekas, J. S., Connerney, J. E. P., Espley, J. R., McFadden, J. P., Mazelle, C., et al. (2016). MAVEN observation of an obliquely propagating low-frequency wave upstream of Mars. *Journal of Geophysical Research: Space Physics*, *121*, 2374–2389. https://doi.org/10.1002/2015JA022306

Ruhunusiri, S., Halekas, J. S., Espley, J. R., Eparvier, F., Brain, D., Mazelle, C., et al. (2018). One-hertz waves at Mars: MAVEN observations. *Journal of Geophysical Research: Space Physics*, *123*, 3460–3476. https://doi.org/10.1029/2017JA024618

Russell, C. T. (1994). *Planetary upstream waves*, *Geophysical Monograph Series* (Vol. 81, pp. 75–86). Washington, DC: American Geophysical Union. https://doi.org/10.1029/GM081p0075

Russell, C. T., Childers, D. D., & Coleman, P. J. (1971). Ogo 5 observations of upstream waves in the interplanetary medium: Discrete wave packets. *Journal of Geophysical Research*, *76*(4), 845–861. https://doi.org/10.1029/JA076i004p00845

Russell, C. T., Luhmann, J. G., Schwingenschuh, K., Riedler, W., & Yeroshenko, Y. (1990). Upstream waves at Mars: Phobos observations. *Geophysical Research Letters*, *17*(6), 897–900. https://doi.org/10.1029/GL017i006p00897

Russell, C. T., Mayerberger, S. S., & Blanco-Cano, X. (2006). Proton cyclotron waves at Mars and Venus. *Advances in Space Research*, *38*(4), 745–751. https://doi.org/10.1016/j.asr.2005.02.091

Sauer, K., & Dubinin, E. (2003). Oscillitons and gyrating ions in a beam-plasma system. *Geophysical Research Letters*, *30*(23), 2192. https://doi.org/10.1029/2003GL018266

Sauer, K., Dubinin, E., Baumgärtel, K., & Tarasov, V. (1998). Low-frequency electromagnetic waves and instabilities within the Martian bi-ion plasma. *Earth, Planets and Space*, *50*(3), 269–278. https://doi.org/10.1186/BF03352113

Sauer, K., Dubinin, E., & McKenzie, J. F. (2001). New type of soliton in bi-ion plasmas and possible implications. *Geophysical Research Letters*, *28*(18), 3589–3592. https://doi.org/10.1029/2001GL013047

Song, P., & Russell, C. T. (1999). Time series data analyses in space physics. *Space Science Reviews*, *87*(3/4), 387–463. https://doi.org/10.1023/A:1005035800454

Song, P., Russell, C. T., & Gary, S. P. (1994). Identification of low-frequency fluctuations in the terrestrial magnetosheath. *Journal of Geophysical Research*, *99*(A4), 6011–6025. https://doi.org/10.1029/93JA03300

Sonnerup, B. U. Ö., & Cahill, L. J. (1968). Explorer 12 observations of the magnetopause current layer. *Journal of Geophysical Research*, *73*(5), 1757–1770. https://doi.org/10.1029/JA073i005p01757

Szegö, K., Glassmeier, K.-H., Bingham, R., Bogdanov, A., Fischer, C., Haerendel, G., et al. (2000). Physics of mass loaded plasmas. *Space Science Reviews*, *94*(3/4), 429–671. https://doi.org/10.1023/A:1026568530975

Thomsen, M. F., Gosling, J. T., Bame, S. J., & Russell, C. T. (1985). Gyrating ions and large-amplitude monochromatic MHD waves upstream of the Earth's bow shock. *Journal of Geophysical Research*, *90*(A1), 267–273. https://doi.org/10.1029/JA090iA01p00267

Trotignon, J. G., Mazelle, C., Bertucci, C., & Acuña, M. H. (2006). Martian shock and magnetic pile-up boundary positions and shapes determined from the Phobos 2 and Mars Global Surveyor data sets. *Planetary and Space Science*, *54*(4), 357–369. https://doi.org/10.1016/j.pss.2006.01.003

Tsurutani, B. T. (1991). Comets: A laboratory for plasma waves and instabilities. In *Cometary plasma processes* (pp. 189–209). Washington, DC: American Geophysical Union. https://doi.org/10.1029/GM061p0189

Wei, H. Y., Cowee, M. M., Russell, C. T., & Leinweber, H. K. (2014). Ion cyclotron waves at Mars: Occurrence and wave properties. *Journal of Geophysical Research: Space Physics*, *119*, 5244–5258. https://doi.org/10.1002/2014JA020067

Wei, H. Y., & Russell, C. T. (2006). Proton cyclotron waves at Mars: Exosphere structure and evidence for a fast neutral disk. *Geophysical Research Letters*, *33*, L23103. https://doi.org/10.1029/2006GL026244

Yamauchi, M., Hara, T., Lundin, R., Dubinin, E., Fedorov, A., Sauvaud, J.-A., et al. (2015). Seasonal variation of Martian pick-up ions: Evidence of breathing exosphere. *Planetary and Space Science*, *119*, 54–61. https://doi.org/10.1016/j.pss.2015.09.013